

178  
3-6-84 050

PPPL-2067

UC20 - F

I-13515

PPPL--2067

DE84 007451

DR# 2144-X

DETERMINATION OF PLASMA ION VELOCITY DISTRIBUTION  
VIA CHARGE-EXCHANGE RECOMBINATION SPECTROSCOPY


By

R.J. Fonck, D.S. Darrow, and K.P. Jaehnig

DECEMBER 1983

**MASTER**

DISTRIBUTION OF THIS DOCUMENT IS UNLIMITED

PLASMA  
PHYSICS  
LABORATORY 

PRINCETON UNIVERSITY  
PRINCETON, NEW JERSEY

PREPARED FOR THE U.S. DEPARTMENT OF ENERGY,  
UNDER CONTRACT DE-AC02-76-CHO-3073.

DETERMINATION OF PLASMA ION VELOCITY DISTRIBUTION  
VIA CHARGE-EXCHANGE RECOMBINATION SPECTROSCOPY

R.J. Fonck, D.S. Darrow, and K.P. Jaehnig  
Plasma Physics Laboratory, Princeton University  
Princeton, New Jersey 08544

ABSTRACT

Spectroscopy of line radiation from plasma impurity ions excited by charge-exchange recombination reactions with energetic neutral beam atoms is rapidly becoming recognized as a powerful technique for measuring ion temperature, bulk plasma motion, impurity transport, and more exotic phenomena such as fast alpha particle distributions. In particular, this diagnostic offers the capability of obtaining space- and time-resolved ion temperature and toroidal plasma rotation profiles with relatively simple optical systems. Cascade-corrected excitation rate coefficients for use in both fully stripped impurity density studies and ion temperature measurements have been calculated for the principal  $\Delta n = 1$  transitions of  $\text{He}^+$ ,  $\text{C}^{5+}$ , and  $\text{O}^{7+}$  with neutral beam energies of 5 to 100 keV/amu. Line intensities and profiles can be affected by atomic fine structure,  $l$ -mixing collisions, motional Stark effects, and product ions created in the neutral beam region which drift into the viewing sightline. General estimates of the importance of these effects for the transitions of interest are provided, along with specific results for the PDX and TFTR tokamaks. A fiber optically coupled spectrometer system has been used on PDX to measure visible  $\text{He}^+$  radiation excited by charge exchange. Central ion temperatures up to 2.4 keV and toroidal rotation speeds up to  $1.5 \times 10^7$  cm/s were observed in diverted discharges with  $P_{\text{INJ}} < 3.0$  MW. The radial profiles of both quantities broaden after the plasma discharge transitions into the ASDEX-like high confinement regime.

*EWG*

## **DISCLAIMER**

This report was prepared as an account of work sponsored by an agency of the United States Government. Neither the United States Government nor any agency thereof, nor any of their employees, makes any warranty, express or implied, or assumes any legal liability or responsibility for the accuracy, completeness, or usefulness of any information, apparatus, product, or process disclosed, or represents that its use would not infringe privately owned rights. Reference herein to any specific commercial product, process, or service by trade name, trademark, manufacturer, or otherwise does not necessarily constitute or imply its endorsement, recommendation, or favoring by the United States Government or any agency thereof. The views and opinions of authors expressed herein do not necessarily state or reflect those of the United States Government or any agency thereof.

## I. INTRODUCTION

The determination of ion velocity distributions in high temperature plasmas is of fundamental importance in controlled fusion research, and several techniques are presently used to measure these distributions to determine, among other quantities, the plasma ion temperature.<sup>1</sup> However, detailed time evolutions and radial profiles of ion temperature have not been routinely available in magnetically confined plasma experiments in spite of their relevance to understanding the confinement properties of particular configurations. This is in contrast to our knowledge of other basic plasma properties such as electron density and temperature profiles, for which radially resolved profiles are often the sine qua non of a reasonable description of the plasma. In addition, given the difficulty in diagnosing hot plasmas, it traditionally has been desirable to make redundant measurements of basic parameters. This is especially true as plasma experiments become larger and more expensive, with correspondingly fewer plasma shots available.

The study of the profiles of spectral lines emitted from hot plasmas has been a time-honored means of obtaining the ion velocity distribution. The Doppler broadened width of the line profile gives a measure of the bulk thermal temperature of the emitting ions if broadening due to mass motion turbulence is negligible,<sup>3</sup> and the shift of a line center gives a measure of the plasma bulk motion, such as may arise in a rotating plasma in a toroidal confinement device.<sup>4</sup> Detailed line shape studies may reveal more exotic information such as the distribution of fast alpha particles in a near-ignition plasma or the presence of nonthermal tails generated by RF heating.<sup>5</sup> Obviously, any of the above measurements presuppose the existence of radiating ions in the hot plasma core whose spatial distributions are

limited and known in a given experiment. Given that such ions exist and can be spatially localized, a detailed knowledge of line excitation mechanisms is then necessary in order to recognize possible distortions of the line profile. These effects may then be compensated for, or preferably, such knowledge may allow one to choose appropriate transitions and ions so as to minimize such distortions.

In this paper, we discuss a relatively new approach to ion velocity distribution measurements in hot plasmas which uses the active spectroscopic technique of Charge-Exchange Recombination Spectroscopy (CXRS).<sup>2</sup> This approach holds promise for providing a relatively simple measurement of ion temperatures with good spatial localization in fusion grade plasmas, and straightforwardly allows time resolved ion temperature profiles in a single plasma shot. Ion temperature and toroidal rotation velocity profiles obtained on the PDX tokamak using CXRS are given as an example of such measurements. Several considerations which affect the validity of CXRS measurements of ion velocity distributions are also addressed.

The application of CXRS to the diagnosis of high temperature plasmas has received much attention in recent years and the rapid maturation of this technique indicates its usefulness. Fonck, Goldston, Kaita, and Post,<sup>2</sup> using results from the PDX tokamak, and Isler and Murray<sup>6</sup> with data from ISX-B, originally discussed the measurements of ion temperature and plasma rotation using CXRS. The basic technique consists of measuring spectral profiles and shifts of emission lines from ions in the plasma which are excited by charge-exchange recombination reactions. Typically, a fully ionized low-Z impurity ion and fast neutral atoms (typically H<sup>0</sup> or D<sup>0</sup>) from either a diagnostic neutral beam or a heating neutral beam are used. The recombination process



leaves the resulting ion in an excited state  $(n, \ell)$  which subsequently decays through photon emission. For common low-Z hydrogenic ions such as  $He^+$ ,  $C^{5+}$ , and  $O^{7+}$ , these spectral lines have wavelengths which range from the extreme ultraviolet to the visible spectral regions. The cross sections for such processes are often large ( $\lambda 10^{-16} \text{ cm}^2$ ) and hence measurable intensities are obtained with moderate neutral densities.

Local impurity ion densities and transport properties of fully stripped low-Z impurities have been studied via reaction Eq. (1) using diagnostic neutral beams in the T-10<sup>7</sup> and PDX<sup>8</sup> tokamaks and using the heating neutral beams in ISX-B.<sup>9</sup> The use of reaction Eq. (1) for the diagnosis of alpha particles has also been discussed.<sup>5, 10</sup> In addition to hydrogen neutral beams, lithium beams are currently in use to study partially ionized charge states of impurities at the plasma edge.<sup>11</sup> In general, fully ionized low-Z impurities are most useful for ion temperature and plasma rotation measurements because naturally occurring impurities such as C and O are fully stripped at tokamak electron temperatures and thus do not strongly radiate and perturb the plasma. In addition, these ions are sufficiently abundant at all radii in the plasma due to cross field transport<sup>8</sup> that no additional contamination of the plasma with impurity atoms is necessary and a full radial profile can be obtained by observing a single spectral line. Measurements of central ion temperature and/or plasma rotation using CXRS have most recently been reported from the PDX,<sup>12</sup> ISX-B,<sup>13</sup> and D-III<sup>14</sup> tokamak groups.

In addition to the CXRS approach described above, several other methods of determining ion velocity distributions in tokamaks presently are

available,<sup>3</sup> but all of these have limitations. The most common measurement is to energy analyze the fast neutrals produced in the center of the plasma by charge exchange with background neutral atoms. This technique measures only the high energy tail of the ion distribution which can escape from the plasma center without re-ionization and it is subject to uncertainties due to ion-orbit effects and nonMaxwellian distributions. As tokamak plasmas become denser, they become increasingly opaque to the central charge-exchange-produced neutrals and the density of background neutrals decrease. Both of these effects result in a reduction of the fast neutral flux escaping from the plasma core region. Thus, a diagnostic neutral beam is necessary to raise locally the central neutral density to give sufficient signal levels and provide good spatial resolution.  $T_i$  may also be determined from analysis of thermonuclear neutron emission, but this again is sensitive primarily to the high energy tail of the ion velocity distribution, and spatial resolution is not yet possible. The calculation of  $T_i$  from neutron emission also presupposes knowledge of the plasma ionic composition. Measurements of the Doppler broadening of impurity line emissions from partially ionized atoms excited by electron impact give measures of the bulk impurity ion energy distribution which can usually be related to the plasma ion temperature quite reliably. The wavelengths of interest for such measurements can lie in the X-ray, extreme ultraviolet, or near ultraviolet spectral regions. If supplementary information on the ion species radial distribution is available (which is not always the case), line profile measurements from several impurity charge states can provide radially resolved  $T_i(r,t)$  measurements. However, it is obviously necessary that a sufficient number of highly ionized heavy atoms which are not fully stripped be present in the hot plasma core, which has  $kT_e \approx 1$  to 5 keV typically. The requirement for a density high

enough to give an adequate signal level may conflict with the need to minimize the heavy impurity concentration. As central electron temperatures increase in the next generation of tokamaks, such as TFTR and JET, so likewise will the atomic number  $Z$  necessary to assure incomplete ionization in the plasma core. The decoupling of impurity ion temperature from the bulk plasma ion temperature must also be considered carefully as  $Z$  increases.

The CXRS measurements of ion velocity distributions are less subject to the limitations mentioned above and will be useful on both the present and next generation of confinement machines with large, hot, dense plasmas. Like other Doppler broadening measurements, the bulk ion temperature is measured. Since low- $Z$  impurities can be used, no heavy impurity injection is necessary, thus reducing the possibility of perturbing the plasma by significantly increasing the impurity content. Furthermore, use of light impurities ensures the measurements will closely reflect the temperature of the bulk plasma. Naturally occurring concentrations ( $n_Z/n_e \sim 1\%$ ) of C and O are quite sufficient for such measurements, and as mentioned earlier, a single spectral line from a single ion species can provide a full radial profile of  $T_i$  since cross-field transport is usually sufficient to ensure fully stripped C and O throughout the plasma. Since the heating neutral beams can often be used for these measurements, the CXRS technique is nonperturbing. Good spatial resolution is obtained by viewing across a collimated neutral beam with a collimated spectrometer, and the radial profile is produced by simply changing the viewing direction of the spectrometer. Thus, the measurement is similar to a crossed beam technique and neither prior knowledge of impurity radial distributions nor Abel inversions are necessary. It has only the relatively minor requirement that optical access to view the beam must be available. Judicious choices of beam injection angle and/or spectrometer viewing



direction allow spatially resolved measurements of plasma rotation in either the toroidal or poloidal directions.

A significant advantage of using CXRS to determine ion velocity distributions is the fact that several of the spectral lines excited by charge exchange have relatively long wavelengths, ranging all the way to the visible spectral range for spectrally isolated  $\Delta n = 1$  transitions between Rydberg states of  $\text{He}^+$  (e.g.,  $\Delta n = 4-3$  at 4686 Å),  $\text{C}^{5+}$  (8-7 at 5290 Å), and  $\text{O}^{7+}$  (10-9 at 6070 Å). These lines are particularly interesting because they allow ion temperature measurements while requiring only radiation-hardened fiber optic access to the reactor vessel. The detectors and spectrometers can be remotely located and shielded. Indeed, initial efforts on PDX and D-III concentrated on HeII 4686Å due to easy visible wavelength access to the tokamak via fiber optics. Even when the visible lines are not bright enough for line profile measurements (a discussion of line intensities follows in Sec. II), sufficiently intense lines will usually lie at  $\lambda > 1000\text{Å}$  and no grazing incidence optics are required. Since typical tokamak plasmas of interest have  $kT_i > 0.5$  keV and the ion mass is low, line widths produced by thermal Doppler broadening are readily resolved with conventional spectroscopic instrumentation.

The use of CXRS to measure ion velocity distributions does, of course, have some limitations and constraints. Fine structure effects and product ion background effects will be discussed in detail in later sections. An obvious requirement is that good beam-spectrometer geometry is needed, and especially with tangential beam injection in toroidal devices, not all radii may be accessible. When several beams intersect the spectrometer line of sight, modulation of a single beam is necessary to obtain good spatial localization. On plasma devices with only RF heating, a diagnostic neutral

beam would be necessary. It should be noted that spectral lines chosen for optimal ion temperature measurements are usually not attractive for absolute impurity density measurements, so another spectrometer would probably be needed for such measurements. Finally, if good absolute intensity results are desired, accurate cross sections and beam particle densities must be calculated for each case of interest.

In this paper, we expand upon our earlier work<sup>2</sup> by discussing a variety of effects that can affect the applicability of CXRS to ion velocity distribution measurements. The emphasis is on estimating these effects to determine when the measurements are valid rather than presenting complete theoretical discussions. For example, a fully rigorous atomic line structure calculation is not performed but estimates are used to evaluate its importance. As an example of the application of this diagnostic technique, we also present the first radial profiles of  $T_i$  and toroidal rotation velocity obtained via CXRS on the PDX tokamak.

The next section discusses the expected line intensities for most  $\Delta n = 1$  transitions of interest for  $\text{He}^+$ ,  $\text{C}^{5+}$ , and  $\text{O}^{7+}$ . The trade-offs between the desire for long wavelengths and high intensities are indicated. Some level-mixing effects which may significantly alter the expected line intensities are also considered. Section III contains a discussion of the influence of atomic fine structure on the determination of bulk ion temperature. Section IV considers the radial delocalization of the observed emissions due to recombined ions drifting into the spectrometer line of sight. This effect is most important in the case of  $\text{He}^+$ , and specific examples for PDX and TFTR are calculated. Finally, Sec. V presents results of measurements of ion temperature and toroidal rotation velocity radial profiles using CXRS with HeII 4686 Å radiation.

We concentrate on discussions of  $\Delta n = 1$  transitions in C and O because these are typically the most abundant impurities in magnetic confinement devices. In addition, He is discussed both because of its long wavelength transitions and its relevance to helium ash measurements. The concentration on low-Z impurities instead of the plasma ions themselves ( $H^+$  or  $D^+$ ) arises from the fact that, in most experiments, there can be an unknown mixture of  $H^+$  and  $D^+$  depending on the particular running conditions. The work presented here can obviously be extended to other low- and high-Z impurities (e.g., Ti or Fe), even to the hard-to-detect He-like charge states of heavy metals (e.g.,  $Fe^{+24}$ ). Finally, we note that a tokamak plasma device will be assumed in all further discussions.

## II. LINE INTENSITIES

The ability to calculate spectral line intensities for CXRS measurements is necessary in order to evaluate which lines to use for specific purposes. While the determination of the density of a fully stripped impurity via CXRS obviously requires knowledge of the total excitation rate for the line measured, it is also important to estimate excitation rates for other lines which may be more suitable for ion velocity measurements (e.g., high  $n$  transitions at long wavelengths) than for impurity density measurements. Estimates of excitation rate coefficients also allow us to determine which line intensities will be dominated by charge exchange rather than electron impact excitation, and hence allow good spatial localization of the emitting source. In this section we discuss excitation rates applicable to CXRS and processes which may alter these rates, especially for long wavelength emissions arising from Rydberg state transitions.

When a spectrometer sightline crosses a neutral beam, the intensity for a transition at wavelength  $\lambda$  due to prompt charge-exchange recombination events is given by

$$B_{\lambda}^{CX} = \frac{1}{4\pi} \sum_{j=1}^N \langle \sigma v \rangle_j^{\lambda} \int n_z n_j^{\lambda} dl \quad (2)$$

where  $\langle \sigma v \rangle_j^{\lambda}$  is the rate coefficient for excitation of wavelength  $\lambda$  by the  $j$ th beam velocity component,  $n_z$  is the impurity ion density, and  $n_j$  is the beam particle component at velocity  $v_j = v_1/\sqrt{j}$ . The summation is over the various beam energy components, and usually  $N = 3$  for hydrogen beams. The intensity contribution from the relatively slow halo neutrals is negligible for most of the considerations in this paper and hence neglected. The integral in Eq. (2) is along the spectrometer line of sight and is replaced by  $n_z n_j^{\lambda} \ell_j$  if the intersection length for the sightline and beam is small. Here,  $\ell_j$  denotes the effective path length of the spectrometer line of sight through the beam for the  $j$ th beam component. If  $\langle \sigma v \rangle_j^{\lambda}$  is in units of  $\text{cm}^3 \text{ s}^{-1}$  and  $n_z$  and  $n_j$  in units of  $\text{cm}^{-3}$ ,  $B_{\lambda}^{CX}$  has the usual intensity units of  $\text{photons}/\text{cm}^2 \times \text{s} \times \text{ster}$ .

It is worth noting as an aside that  $B_{\lambda}^{CX}$  in general does not depend on the electron temperature, and one can expect to observe ions in regions of the plasma where  $T_e$  is too low to excite the transitions via electron collisions (i.e., near the plasma edge). This also eases the uncertainties in calculating local impurity densities  $n_z$ .

The problem of calculating  $B_{\lambda}^{CX}$  consists of calculating  $n_j \ell_j$  and  $\langle \sigma v \rangle_j^{\lambda}$  for specific cases. The beam particle column densities are readily calculated via a beam attenuation code, given specific plasma density and temperature profiles and a specific beam-spectrometer geometry. These calculations use the total stopping cross sections used in Ref. 15 and are not discussed further here except as the results are applied to specific cases of interest.

Several theoretical techniques are used to calculate the cross section  $\sigma(n,\ell)$  for populating a given atomic level with principal quantum number  $n$  and orbital angular momentum number  $\ell$  after a charge-exchange collision, with different techniques appropriate for different energy ranges.<sup>16</sup> The calculation of specific values of  $\sigma(n,\ell)$  for given energy ranges is presently a very active area of theoretical atomic physics, and values for a wide range of beam energies are becoming available. Only some of this work will be referenced in this paper as it is needed. A few general features of these results are worth noting however. The charge-exchange reaction tends to be a resonant process in that the electron from the beam neutral particle prefers to transfer to excited levels in the product ion  $[A^{Z-1}]$  in Eq. (1) which preserve its orbital energy and radius.<sup>17</sup> This leads to a peaking of  $\sigma(n) = \sum_{\ell} \sigma(n,\ell)$  in  $n$  with  $n_{\text{Max}} \approx Z^{3/4}$ . As the beam energy increases, the width of this distribution in  $n$  increases and higher  $n$  levels are populated. The  $\ell$ -distribution of  $\sigma(n,\ell)$  for a given  $n$  level also is peaked, with  $\sigma(n,\ell)$  increasing sharply as  $\ell$  increases for  $n \lesssim n_{\text{Max}}$  and tending to level off or peak at  $\ell \sim n_{\text{Max}}$  for  $n > n_{\text{Max}}$ . Thus, for transitions between states near or below  $n_{\text{Max}}$ , the high  $\ell$  (YRAST) states are predominately populated and the subsequent  $\Delta n = 1$  decay transitions are the most intense. The charge-exchange reaction produces very little momentum change for the recombined ion and hence does not disturb the ion velocity distribution.

The observed intensities are determined by the cascade of the excited electrons from their initial distribution produced by the charge-exchange reaction, and this of course results in a line intensity pattern that does not at first glance look like the initial  $\sigma(n,\ell)$  distribution given by theory. For example, Fig. 1(a) shows schematically the distribution of  $\sigma(n,\ell)$  for a given case of  $H^{\circ} + C^{6+} + H^{+} + C^{5+}(n,\ell)$  as calculated by Shipsey, Greene, and Browne.<sup>18</sup> The cascade-corrected cross section for the  $(n,\ell)$  state is given by

$$\sigma_c(n, \ell) = \sum_{k=1}^N \sum_{\ell_k=0}^{n+k-1} [b_{n, \ell; n+1, \ell_1} b_{n+1, \ell_1; n+2, \ell_2} \dots b_{n+k-i, \ell_{k-1}; n+k, \ell_k} \sigma_d(n+k, \ell_k)] \quad (3)$$

where  $\sigma_d(n, \ell)$  is the direct charge-exchange cross section and  $b_{n\ell; n'\ell'}$  is the branching ratio for electric dipole transitions from state  $n'\ell'$  to  $n\ell$  (note that  $b_{n\ell; n'\ell'} = 0$  unless  $\ell' = \ell \pm 1$ ). These branching ratios for hydrogenic atoms are readily calculated using standard references. The sum in Eq. (3) is terminated at some large value of  $n = N$ , beyond which  $\sigma_d$  is negligible. The cascade-corrected cross sections for the case in Fig. 1(a) are shown in Fig. 1(b). Since atomic fine structure usually is not resolved, we are interested in the total effective cross section for excitation of a given  $n' \rightarrow n$  transition which is given by summing over all the  $\ell$  levels with the appropriate branching ratios. These cross sections are given by

$$\sigma(n, n') \equiv \sigma^\lambda = \sum_{\ell=0}^{n'-1} \sigma(n', \ell) b_{n\ell; n'\ell'} \quad (4)$$

with  $\ell = \ell' \pm 1$ . Figure 1(c) shows these resultant total cross sections for line excitation for the case of Fig. 1a. The transitions between lowest  $n$  levels will be brightest and will have intensities which are least sensitive to the original  $\sigma_d(n, \ell)$  distribution. These features make the short wavelength transitions between low  $n$  states most attractive for impurity density measurements since the  $\langle \sigma v \rangle^\lambda$  rates can be reliably calculated.

Since these cascade calculations are somewhat tedious and the results are needed for several CXRS applications, we present in Figs. 2-6 total effective rate coefficients for excitation via charge exchange for the important  $\Delta n = 1$  transitions of HeII, CVI, and OVIII, using values of  $\sigma_d(n, \ell)$  provided by several authors. The results of Shipsey, Greene, and Browne<sup>18</sup> for  $H^0 + O^{8+}$  were obtained using the perturbed stationary state method including molecular states for the specific system of interest and are the most accurate for this energy range. The more general Unified Distorted Wave Approximation (UDWA) calculations of Ryufuku and coworkers,<sup>20,21</sup> while not as exact, provide  $\sigma_d(n, \ell)$  over a very wide range of beam energy,  $Z$ , and  $n$ , thus being most useful for global estimates of intensities. The curves drawn in Figs. 2-6 are our interpolations between the few points in energy for which the  $\sigma_d(n, \ell)$ 's are provided. The tendency for the long wavelength higher  $n$  transition to be excited only at high beam energies is evident in these results, as is the tendency for cross sections to peak at values of  $n_{\text{Max}} \sim Z^{3/4}$ . For example, the excitation rate coefficient for transitions drop rapidly as  $n$  increases above  $n = 2$  in HeII, while the sharp drop in  $\langle \sigma v \rangle^\lambda$  for CVI does not appear until  $n \gtrsim 5$ .

While the theoretical cross sections  $\sigma_d(n, \ell)$  provide the populations of a given state via direct charge-exchange events, the cascade process can be significantly affected by the surrounding plasma environment. Several processes, can cause transfer between different  $\ell$ -levels before an electron drops to lower states via photon radiation. These  $\ell$ -mixing processes can cause a distortion of the relative populations among the excited states and affect line intensities and fine structure line profiles. Other effects, such as ionization of the ion from the excited states before photon emission, tend not to be important for typical tokamak plasmas; we discuss only collisional

$l$ -mixing and possible  $l$ -mixing due to the motional Stark effect<sup>22</sup> produced by ion thermal motion in the magnetic field. As mentioned earlier, the emphasis here is on obtaining estimates as to when these  $l$ -mixing processes are important rather than providing a rigorous theoretical discussion of their details.

The  $l$ -mixing effects of ion-ion collisions have been discussed by Pengelly and Seaton<sup>23</sup> for planetary nebulae with  $N_e \approx 10^4 \text{ cm}^{-3}$  and  $kT_e \approx kT_i = 1 \text{ eV}$ , and we simply expand on their discussion to include a plasma regime typical of contemporary fusion experiments ( $N_e \approx 10^{13} - 10^{14} \text{ cm}^{-3}$ ,  $kT_i \approx 1-10 \text{ keV}$ ). They use an impact parameter collision model with straight line trajectories to derive the net rate coefficients for transitions between nearly degenerate  $l$ -states due to charged particle collisions. We follow their discussion to extrapolate the results to our regime of interest. The rate coefficient for  $n\bar{l} + n\bar{l}'$  ( $l' = l \pm 1$ ) transitions between nearly degenerate states in hydrogenic ions with charge  $Z$  and due to collisions with ions of charge  $z$  is given by

$$q_{n\bar{l}}^{Z,z} = 9.93 \times 10^{-6} \left(\frac{\mu}{m}\right)^{1/2} \frac{D_{n\bar{l}}}{\tau_i^{1/2}} \left\{ 11.54 + \log_{10} \left( \frac{\tau_i^m}{D_{n\bar{l}} \mu} \right) + 2 \log_{10} \frac{\bar{R}_c}{R_c} \right\} \text{ cm}^3 \text{ sec}^{-1} \quad (5)$$

where

$$D_{n\bar{l}} = \left(\frac{z}{Z}\right)^2 6 n^2 (n^3 - l^2 - l - 1) , \quad (6)$$



$\mu$  is the reduced ion mass of the colliding particles,  $T_i$  is the ion temperature in  $^{\circ}\text{K}$ , and  $m$  is the electron mass. If the Debye radius is used as a cutoff length for the collisional interaction, the last term in Eq. (5) is given by

$$2 \log_{10} \bar{R}_c \approx 1.68 + \log_{10}(T_i/N_e) \quad (7)$$

with  $N_e$  being the electron density in units of  $\text{cm}^{-3}$ .

Assuming  $m_z = 2Zm_p$  and  $m_{\bar{z}} = 2zm_p$  where  $m_p$  is the proton mass, we find that for  $z, \bar{z} < 10$ ,  $n < 20$ , and  $kT_i < 10$  keV, within a variation of only  $\pm 26\%$ ,

$$q_{nl}^{z,\bar{z}} = q_{nl}^{H,H} \frac{Z\bar{z}}{Z+\bar{z}} \left(\frac{z}{\bar{z}}\right)^2 \frac{0.091}{\sqrt{T_i}} \quad (8)$$

where  $T_i$  is in keV and  $q_{nl}^{H,H}$  is the proton-proton  $\ell$ -mixing rate calculated by Pengelly and Seaton for  $N_e \approx 10^4 \text{ cm}^{-3}$  and  $T \approx 1$  eV. This form allows their numerical results for  $q_{nl}^{H,H}$  to be scaled directly to the present cases of interest. If several ion species are present, the total reaction rate for  $\ell$ -mixing transitions from state  $(n, \ell)$  to  $(n, \ell \pm 1)$  is given by

$$\begin{aligned} \sum_z N_z q_{nl}^{z,\bar{z}} &= q_{nl}^{H,H} \frac{0.091}{z^2 \sqrt{T_i}} \sum_z N_z z^2 \sqrt{\frac{Z\bar{z}}{Z+\bar{z}}} \\ &\approx q_{nl}^{H,H} \frac{0.106}{\sqrt{T_i}} \frac{1}{z^2} \sum_z N_z z^2 \end{aligned} \quad (9)$$

where the square root term in the sum has been replaced by its median value assuming  $z$  and  $Z$  range from 1 to 10. For  $z$  and  $Z \leq 10$ ,  $n \leq 20$ , and  $T_i \leq 10$  keV, the relation in Eq. (8) is accurate to  $\pm 68\%$ . If heavy impurities have negligible densities, the sum in Eq. (9) is just the product  $N_e Z_{\text{eff}}$  where  $Z_{\text{eff}}$  is the usual resistivity anomaly factor, and Eq. (9) reduces to

$$\sum_z N_z q_{nl}^{Z,z} = q_{nl}^{H,H} \frac{0.106}{\sqrt{T_i}} \frac{Z_{\text{eff}}}{Z^2} N_e \approx (\tau_{nl}^Z)^{-1} \quad (10)$$

The  $l$ -levels can be considered to be mixed collisionally when  $\lambda_{nl}^Z \tau_{nl}^Z = 1$  where

$$\lambda_{nl}^Z = Z^4 \lambda_{nl}^H \quad (11)$$

is the total spontaneous emission rate out of the  $(n,l)$  level. For complete  $l$ -mixing of a given  $n$ -level, a sum over all  $l$ -values must be made, and the resulting critical value of  $N_e$  above which a particular  $n$  level will be mixed collisionally is given by

$$N_e(n) \frac{Z_{\text{eff}}}{Z^6} \frac{0.106}{\sqrt{T_i}} = \frac{1}{\tau_n^H q_n^H} \quad (12)$$

This result shows that we can replace the critical  $N_e$  given by Pengelly and Seaton for a given  $n$ -level by the quantity on the left side of Eq. (12) to estimate the  $n$ -levels which are mixed in our denser, hotter plasmas. This procedure eliminates the need to reproduce the laborious evaluations of excitation and spontaneous emission rates for each case. Since  $\tau_{n,l} \sim n^3$  and  $q_{n,l} \sim n^{3-4}$  [cf., Eq. (5)], the critical density for a given sublevel  $(n,l)$  varies roughly as  $n^{-6}$  and one expects this criterion for  $l$ -mixing to be

fairly sharp in  $n$ . Using the results from Fig. 4 of Pengelly and Seaton, which plots the critical density  $N_{e,c}(n)$  as a function of  $n$ , we use Eq. (12) to produce Fig. 7, which plots the critical value of  $N_e$  (in units of  $10^{13} \text{ cm}^{-3}$ ) as a function of  $n$ . If, for a given case, the value of the ordinate lies above the curve for a given  $n$ -level, collisional  $\ell$ -mixing can be neglected to lowest order, while a statistical distribution among  $\ell$  states can be assumed if the value falls below the curve. For example, with  $N_e = 2 \times 10^{13} \text{ cm}^{-3}$ ,  $T_i = 1 \text{ keV}$ , and  $Z_{\text{eff}} = 2$  (typical PDX parameters halfway out from the center), all levels with  $n \gtrsim 5$  for carbon and  $n \gtrsim 6$  for oxygen can be considered to be mixed collisionally, and the relative population among the various  $\ell$ -states in a given  $n$ -level is then given by their statistical weights  $(2\ell + 1)/n^2$ .

Before examining the consequences of this  $\ell$ -mixing on the rate coefficients, we consider a second  $\ell$ -mixing process which can be dominant in certain parameter regimes. As an ion gyrates around a magnetic field line, it sees an electric field in its own frame which is perpendicular to the magnetic field direction and whose magnitude is given approximately by

$$F_{v \times B} = vB = 2.20 \times 10^5 \left( \frac{T_i}{2} \right)^{1/2} B \text{ (V/m)} \quad (13)$$

where the ion thermal speed is used and  $T_i$  is in keV and  $B$  in Teslas. Clearly, large fields can be experienced and the atomic Stark effect acts to mix states of different parity (i.e.,  $2$ ). Since both Zeeman and Stark splitting of the various atomic sublevels are simultaneously present, the situation can become rather complex as  $n$  increases and the perturbations become comparable to the energy spacing between adjacent fine structure levels. It is just this strong mixing regime which is of interest for gaining estimates for critical  $n$ -levels above which this motional Stark effect can

cause severe  $l$ -mixing. The problem is not nearly as amenable to straightforward calculation as was the collisional  $l$ -mixing case, but a crude treatment does allow progress to be made. In the spirit of other qualitative treatments of strong field mixing regimes in atomic structure, we obtain an estimate for the onset of Stark mixing between different  $l$ -states by comparing the energy shift due to the motional Stark field to the field-free fine structure energy differences.

Ignoring nuclear mass effects and Lamb shifts, the energy of a given level in a hydrogenic ion with nuclear charge  $Z$ , principal quantum number  $n$ , and total angular momentum  $j$  is given by<sup>24</sup>

$$E(n, j) = -Ry \frac{Z^2}{n^2} \left[ 1 + \frac{(\alpha Z)^2}{n} \left( \frac{1}{k} - \frac{3}{4n} \right) \right] \quad (14)$$

where  $Ry$  is the Rydberg energy (13.6 eV),  $\alpha$  is the fine structure constant, and  $k = j + 1/2 = 1, 2, \dots, n$ . Then the energy splitting between fine structure states in the same  $n$ -level with  $j$  values differing by 1 is

$$\Delta E_{FS} = -Ry \frac{\alpha^2 Z^4}{n^3} \frac{1}{k(k+1)}. \quad (15)$$

In the limit where the Stark shifts are much larger than the fine structure separation, the  $n$ -manifold splits into a series of equally spaced levels which have a total energy separation of<sup>25</sup>

$$\Delta E_S = 3 Ry F \frac{4\pi\epsilon_0 a_0^3}{e^2} \frac{n(n-1)}{Z} \quad (16)$$

where  $F$  is the applied electric field and  $a_0$  is the Bohr radius. Of course, severe  $l$ -mixing occurs long before this Stark pattern fully develops. We estimate when  $l$ -mixing will start by solving for the  $n$ -value at which the fine structure separation is equal to the energy shift of the electron due to the motional electric field.

As  $T_1$  or  $B$  increases, the motional Stark effect first arises as a second order perturbation in the energy of magnetic sublevels of a given  $j$ -manifold.<sup>26</sup> This occurs because the electric field is perpendicular to the magnetic field and couples states through the  $\langle njm|x|njm' \rangle$  matrix elements with the selection rule  $m' = m \pm 1$  (or  $m'_z = m_z \pm 1$ ) assuming the  $B$ -field is along the  $Z$ -axis. But these  $m$  levels are no longer degenerate due to the presence of the magnetic field, and one thus returns to a quadratic Stark effect instead of the usual hydrogenic linear Stark effect. That is, the atom in the magnetic field has no electric dipole moment perpendicular to the field even though, in the absence of the magnetic field, the  $j$  degeneracy of the energy levels allows a net dipole moment to exist.

The resulting second order shift due to the motional Stark field is given by

$$\Delta E^Q = \frac{|\langle njm | e x F_{yxB} | njm' \rangle|^2}{2\mu_B} = (eF_{yxB})^2 \frac{n^4 a_0^2}{Z^2 \mu_B} \quad (17)$$

where we have approximated the matrix element of  $x$  by the size of the Bohr radius for the  $n$ th excited state. In Eq. (17),  $\mu_0$  is the Bohr magneton. Equating  $\Delta E^Q$  with the spacing between the most closely spaced field-free fine structure levels yields a rough estimate of the minimal  $n$ -level for the onset of  $l$ -mixing. Combining Eqs. (15) (with  $k = n$ ) and Eq. (17), we get for  $n \gg 1$

$$n_S^Q = 2.04 \left( \frac{Z^7}{T_1 B} \right)^{1/9}, \quad (18)$$

with  $T_1$  in keV and  $B$  in Teslas. Stark mixing of  $l$ -levels can be considered important for all  $n > n_S^Q$ . This estimate is, of course, crude and somewhat pessimistic since we only require that the Stark shift equal the minimal fine structure spacing, but it does illustrate the general features that  $n_S^Q$  depends almost linearly on  $Z$  and very weakly on  $T_1$  and  $B$ .

Since we are in a regime where the motional Stark field can be large (due to high  $T_1$  and  $B$ ), and since, with a  $B$  of several Tesla, the magnetic perturbation of the field-free energy levels can approach the fine structure separation, the motional Stark effect may in fact be more linear than quadratic in the magnetic field strength. As  $n$  increases, the Zeeman shift of a given  $m_j$  level

$$\Delta E_Z = m \mu_0 B, \quad (19)$$

becomes comparable to  $\Delta E_{FS}$  and the Paschen-Bach regime is attained. Thus states with  $\Delta m = \pm 1$  can approach degeneracy with respect to the Stark perturbation. Ignoring the Zeeman splitting, the energy separation between previously degenerate levels with  $j = n/2$  due to an electric field  $F$  is given by<sup>24</sup>

$$\Delta E^L = 3 \frac{3}{4} \frac{n}{Z} Ry \frac{4\pi\epsilon_0 a_0^3}{e^2} F. \quad (20)$$

Using the motional Stark field for F, and equating this shift to the minimal fine structure separation gives

$$n_S^L = 1.91 \left( \frac{Z^{11}}{T_1 B^2} \right)^{1/12}, \quad (21)$$

as an estimate of the critical value of n at which l-mixing due to the motional Stark field may become important. Again, a near linear dependence on Z and weak dependence on  $T_1$  and B are evident.

The critical n values for Stark mixing given by Eqs. (18) and (21) are plotted in Fig. 8, and the interpretation of the plots is similar to that for the collisional l-mixing case. For a given Z,  $T_1$ , and B, any n values to the right of the curve can be considered to have the l-levels mixed while those to the left will be unmixed. Unlike the collisional case, the criteria for l-mixing is not well-defined. The two values of  $n_c$  in Fig. 8 are quite close to one another, and to evaluate the importance of Stark mixing compared to collisional l-mixing, we take whichever is lower for given plasma conditions as our criterion for whether a given n level has significant Stark mixing. For  $T_1 \sim$  few keV,  $B = 2$  T, and  $Z = 2$  to 8, one readily concludes that collisional mixing is still the dominant process for causing a mixing of l-level populations at the lowest possible n values. However, it seems possible that Stark mixing may become important at conditions with high temperature, high field strength, and low density.

The consequences of severe  $l$ -mixing on the rate coefficients for charge-exchange excitation are estimated by insisting that above some critical level  $n_c$ , given by Figs. 7 and 8, the  $l$ -levels for a given  $n$ -state are fully coupled [with relative populations  $(2l + 1)/n^2$ ] during the cascade process. For typical PDX parameters, we have  $n_c = 2$  for  $\text{He}^+$ ,  $n_c = 5$  for  $\text{C}^{5+}$ , and  $n_c = 6$  for  $\text{O}^{7+}$ , and the rate coefficients plotted in Figs. 2, 4, and 6 are recalculated and plotted in Figs. 9, 10, and 11 with statistical distributions imposed during the cascades for all  $n > n_c$ . For  $n > n_c$ , the preferred coupling of the low  $l$ -levels to the lowest energy states and the strong coupling of all  $l$ -levels to one another in the excited state causes a larger fraction of the electrons to drain through the  $\Delta n > 1$  channels than would do so in the absence of  $l$ -mixing. Likewise, a drop in excitation rates for  $\Delta n = 1$  transitions out of the lower states occurs with  $l$ -mixing at high  $n$  because the cascading electron distribution has shifted to lower  $l$  values and the  $\Delta n > 1$  transitions are then energetically preferred. As can be seen by comparing Figs. 2-6 and 9-11, the overall effect of  $l$ -mixing is to reduce the rate coefficients for most of the  $\Delta n = 1$  transitions, especially for  $n > n_c$ .

The results presented here are necessarily qualitative due to the simple model used for  $l$ -mixing, but they do illustrate the importance of more detailed studies of the influence of collisional mixing on CXRS. It is interesting to note that the  $\Delta n > 1$  transitions can be most affected by  $l$ -mixing. For example, at 25 keV/amu, the 7-3 transition in  $\text{O}^{7+}$  is 2.7 times more intense with  $l$ -mixing than without while the 3-2 transition has a corresponding ratio of 0.65, resulting in an intensity ratio change of  $> 4$  above that expected without  $l$ -mixing for  $n > 6$ .

A further consequence of the presence of  $l$ -mixing effects is the general principle that the lowest accessible  $\Delta n = 1$  transitions are best suited for accurate fully stripped impurity density measurements using CXRS.



This is so because the cascade process tends to wash out uncertainties in the  $(n, \ell)$  distributions at high  $n$  and hence the lower  $\Delta n = 1$  transitions are least affected by a lack of precise knowledge of the direct  $(n, \ell)$  distributions and  $\ell$ -mixing effects at high  $n$ .

Finally,  $\ell$ -mixing processes can substantially alter the intensity of light emitted by the plasma due to electron excitation of the hydrogenic ions which will inevitably be present in the cooler plasma periphery. Since this radiation is at the same wavelength as that excited by prompt charge exchange, it can be a source of considerable complication in interpreting signals from the spectrometer. Of course, modulation of the neutral beam (as in Ref. 8) or spectral line profile discrimination (see Sec. V) can be used to distinguish between prompt charge-exchange radiation and background plasma light from the plasma edge, but the charge-exchange process itself creates ions which can be excited via electron impact and thus change the expected line intensity. Modulation of the beam will not help distinguish between this electron excitation component and the direct charge-exchange component. Since electron excitation of high  $n$  levels of  $C^{5+}$  and  $O^{7+}$  is negligible (due to their high excitation energies from the ground state) whereas charge-exchange cross sections peak at large  $n$ , electron excitation of  $\Delta n = 1$  lines in  $C^{5+}$  or  $O^{7+}$  is usually negligible with respect to prompt charge exchange at high  $n$  values. Indeed, it is only with charge-exchange excitation that these transitions are observed at all in tokamak plasmas. However, for very low- $Z$  elements such as He or Li, the charge-exchange cross sections tend to peak at  $n = 2$  and drop rapidly as  $n$  increases ( $\sigma \sim 1/n^3$ ). The threshold energy for electron impact excitation of higher  $n$  levels is small enough that electron excitation rates are comparable to charge-exchange rates, contrary to the case for higher  $Z$ . This is discussed in some detail later, but we note here that  $\ell$ -mixing can

significantly increase the electron impact excitation rate of  $\Delta n = 1$  transitions by moving the excited electron from the  $np^2P$  state (which will decay back to the ground state with high probability) to higher  $l$ -states which will then decay to intermediate levels. For example, the electron excitation of the HeII 4-3 transition at 4686 Å via excitation of the  $n = 4$  level from the ground state can be enhanced by an order of magnitude if the  $n = 4$  level is heavily mixed. This result has implications for the use of such transitions for ion temperature measurements and for the study of He<sup>++</sup> ash in tokamak devices, and will be referred to later.

### III. FINE STRUCTURE EFFECTS ON THE LINE PROFILE

The ability to determine the ion velocity distribution via CXRS depends on the line shape being determined predominately by Doppler effects. For an ion species with a Maxwellian distribution and temperature  $kT_i$  in keV, the full width at half maximum (FWHM) of the gaussian line shape is given by

$$\Delta\nu_D = \nu \cdot 1.73 \times 10^{-3} \sqrt{\frac{T_i}{Z}} \quad (22)$$

where  $\nu$  is the wavenumber of the transition,  $T_i$  is in keV and the ion mass is taken to be  $2Zm_p$ . For  $\Delta n = 1$  transitions in hydrogenic ions, the wavenumber of the emitted photons is given by Eq. (14) to be

$$\nu = \frac{2Z^2 R_y}{n} \quad (23)$$

for high  $n$  values. Using Eqs. (19), (22), and (23) one can readily conclude that the unresolved Zeeman splitting is negligible compared to Doppler broadening for  $T_i =$  few keV and  $B = 1$  to 5 T. Likewise, motional Stark

broadening is almost always much less than the Doppler width. Although Zeeman and Stark broadening of a line are less than the total separation of fine structure components for our range of  $n$  and  $Z$ , one has to evaluate whether the unresolved fine structure itself may give rise to incorrect temperature measurements. Any such effect will be most pronounced at low  $T_i$  where the Doppler broadening is small. Temperatures measured near the edge of the plasma will thus be most influenced by this effect. Even if the FWHM of a line profile gives a good measure of  $T_i$ , subtleties in the line wings can be mistakenly attributed to nonthermal ion velocities. To assess the magnitude of these effects, we calculate the total line profiles which arise from a superposition of gaussian line shapes centered at the position of the fine structure components. These profiles then allow us to calculate correction factors to be applied to  $T_i$  measurements when Eq. (22) is used to derive  $T_i$  from the FWHM. Since atomic fine structure is often the dominant broadening mechanism for the unresolved manifold of lines, we neglect Zeeman splitting and use the field-free energy levels.

The energy level of discrete  $(n, j)$  states of hydrogenic ions has been tabulated to high accuracy by Garcia and Mack<sup>27</sup> and we use these values to evaluate the wavelengths of all electric dipole transitions between states with  $\Delta n = 1$ . The relative intensities of given fine structure transitions are obtained by using the cascade corrected cross sections for excitation via charge exchange as given by Eq. (3) and including  $l$ -mixing in higher  $n$  levels where appropriate. The population of different  $j$ -levels of the upper state is obtained from the cascade corrected  $l$ -distribution and the Burger-Dorgelo-Ornstein sum rule.<sup>28</sup> Samples of the resulting intensities and position of fine structure components are shown in Fig. 12, along with the same transitions each having a gaussian profile due to Doppler broadening. The sum

of all the fine structure components is the overall envelope and represents the actual measured profile. Using the FWHM of the composite line profile from such calculations, we define an apparent ion temperature given by Eq. (22) and this FWHM. The ratio of the real temperature to this apparent value gives the correction factor by which experimental values of  $T_i$  should be multiplied to arrive at the actual ion temperature. These ratios for all  $\Delta n = 1$  transitions of interest of  $\text{He}^+$ ,  $\text{C}^{5+}$ , and  $\text{O}^{7+}$  are shown in Figs. 13 to 15 for beam energies of 25 keV/amu, and using the  $\sigma_d(n, \ell)$  values of Ryufuku.<sup>21</sup> Full  $\ell$ -mixing was assumed for  $n > n_c$ , where  $n_c = 2, 5,$  and  $6$  for  $\text{He}^+$ ,  $\text{C}^{5+}$ , and  $\text{O}^{7+}$ , respectively. The large discontinuities in the curves for some transitions (e.g., 4-3 of  $\text{C}^{5+}$ ) are due to the merging of the profiles of discrete fine structure transitions as  $T_i$  increases and the Doppler width becomes larger than the transition separation. The closer the correction factor is to 1.0, the more symmetric and gaussian-like the sum profile is. In general, the higher wavelength transitions are least susceptible to distortion by fine structure at high  $T_i$  and thus most suited for determining  $T_i$ . These results can change by up to  $\sim 10\%$  depending on whether  $\ell$ -mixing is included in the upper levels or not. The  $\ell$ -mixing tends to broaden the line structure by increasing the intensity of widely separated fine structure components originating from moderate to low  $\ell$ -levels. However, since the high  $n$  transitions which are preferred for  $kT_i$  measurements are also those which originate from transitions out of  $\ell$ -mixed states, these curves provide a reasonable correction factor for  $T_i$  measurements which can be applied over a very wide parameter range.

A few obvious conclusions can be drawn from these results. The low-lying transitions are not well-suited for ion temperature measurements unless the fine structure components themselves are resolved. Transitions between high  $n$  states are much better but, as noted earlier, the charge-exchange cross

sections drop rapidly as  $n$  increases. Helium is almost ideal due to its low mass and relatively bright visible line, but this 4-3 transition is best excited by neutral beams with a high primary beam energy ( $> 60$  keV/amu) so that all three beam energy components contribute to the CXRS signal. On the other hand, measurements using helium are most prone to errors arising from ions drifting into the spectrometer line of sight (see the next section). The visible lines of  $C^{5+}$  and  $O^{7+}$  are also attractive candidates except that, again, higher beam energies are desirable for reasonable intensities. Also, overlap with visible lines of HI and other impurity ions tend to make several of these lines questionable for reliable ion temperature measurements in the visible range unless the beam is modulated. The 60 to 90 keV/amu beam energies planned for the TFTR tokamak may make these lines quite attractive for simple fiber optically coupled spectrometer systems. For smaller tokamaks such as PDX and PLT with 20 to 50 keV/amu neutral beams, the near UV lines of  $C^{5+}$  and  $O^{7+}$  are most attractive for ion temperature measurements when  $He^{++}$  is not present in the plasma.

#### IV. RADIATION FROM PRODUCT IONS

Finally, we consider the effects of hydrogenic ions which are produced by the neutral beam out of the spectrometer line of sight and subsequently drift into the sightline as they follow the toroidal field lines. Consider a typical experimental situation as depicted in Fig. 16, wherein a neutral beam is injected in the plasma midplane with a tangency radius of  $R_{BT}$ . A spectrometer sightline, also in the plasma midplane with tangency radius  $R_{ST}$  intersects the beam at a major radius of  $R_I$ . Since hydrogenic ions are produced via reaction Eq. (1) along the entire beam line, there is a source of hydrogenic ions at all  $R$  that may be able to drift around the torus into the

view of the spectrometer. For example, ions with charge  $Z-1$  created in the beam volume near point A in Fig. 16 can follow the indicated trajectory to cross the spectrometer sightline before being ionized back to charge state  $Z$ . If the emission due to electron collisional excitation of these drifting ions, integrated along the spectrometer sightline, is comparable to the localized prompt charge-exchange emission at  $R = R_I$ , an erroneous ion velocity distribution (and/or fully stripped impurity density) will be derived since one is sampling ions created over a large range of  $R$ . This problem is most severe for lower  $Z$  elements since the excitation energies of the charge-exchange induced transitions are very low. It is especially relevant for measuring thermal He ash densities or for CXRS temperatures based on  $\text{He}^{++}$ . Unlike interfering radiation from the cool plasma periphery, this electron excited component from radii different than  $R_I$  cannot be discriminated against by modulating the beam since it will be in phase with the beam just as the prompt charge-exchange signal will be.

An estimate of the magnitude and radial extent of the electron excited signal is given by a relatively simple model. The intensity of light at wavelength  $\lambda$  due to electron excitation out of the ground state is given by

$$B_{\lambda}^{e-} = \frac{1}{4\pi} \int_L N_e(R) n_{Z-1}^{CX}(R) Q_{1s-np}^{Z-1}(R) b_{\lambda} d\ell \quad (24)$$

where  $Q_{1s-np}$  is the electron excitation rate for the  $1s-np$  transition,  $b_{\lambda}$  is the branching ratio for the transition of interest, and  $n_{Z-1}^{CX}$  is the density of ions produced by charge exchange between the beam neutrals and ions with charge  $Z$  at a radius  $R$ . The integral in Eq. (24) is along the entire path that the spectrometer line of sight takes through the plasma. (For ease of calculation, we treat all plasma parameters as a function of major radius

R). We express  $n_{Z-1}^{cx}$  as a function of the value it attains in ionization charge-exchange equilibrium in the beam volume:

$$n_{Z-1}^{cx} = \xi(R) \frac{n_Z(R)}{N_e(R) I_{Z-1}(T_e)} \sum_{j=1}^3 n_j \langle \sigma v \rangle_j^T \quad (25)$$

where  $n_Z$  is the density of ions with charge state  $Z$  at a major radius of  $R$ ,  $N_e$  is the electron density,  $I_{Z-1}(T_e)$  is the ionization rate coefficient for the  $Z-1$  ion species,  $n_j$  is the density of beam neutrals with energy  $E_0/\sqrt{j}$ , and  $\langle \sigma v \rangle_j^T$  is the total recombination rate coefficient of the  $Z$  ion species due to charge exchange. The proportionality factor  $\xi(R)$  depends on the parallel transport of the recombined ions along the field lines and the particular beam-spectrometer geometry being used, and is discussed in more detail below. Since we are usually interested in fully stripped low- $Z$  impurities in hot plasmas, it is reasonable to assume that  $n_Z$  is roughly proportional to the electron density,  $n_Z(R) = N_e(R) \times \text{constant}$ .

Assuming a relatively narrow neutral beam so that the integral in Eq. (2) can be replaced by average values, the ratio of the radiation due to the ions drifting into the spectrometer sightline (which we henceforth refer to as the ion "plume" intensity) to the prompt charge-exchange signal at the same wavelength is given by

$$\frac{B_\lambda^{e-}}{B_\lambda^{cx}} = \frac{1}{N_e(R_I) \sum_{j=1}^3 \{ (n_\lambda(R_I))_j \langle \sigma v \rangle_j^\lambda \}} \times \int_L N_e(R) \xi(R) \frac{Q^{Z-1} 1s-np(R) b_\lambda}{I_{Z-1}(T_e)} \left[ \sum_{j=1}^3 n_j \langle \sigma v \rangle_j^T \right] d\ell \quad (26)$$

Note that this ratio is independent of the beam power since  $n_j$  is in both the numerator and denominator. Hence this plume emission can be significant even if the beam power itself is not sufficient to change the overall ionization balance of the impurities. That this ratio can easily be significant may be seen by noting that, at least for 2-1 transitions, the electron excitation rate roughly equals the ionization rate while the total charge-exchange rate is always greater than or equal to the rate for exciting a given transition. The plume-to-prompt ratio then reduces approximately to the ratio of  $N_e$ , weighted by  $\xi$  and integrated along the entire spectrometer line of sight, to the value of  $N_e$  at the intersection point times the beam width.

The plume attenuation factor  $\xi(R)$  is estimated by considering the transport of ions along the magnetic field lines. This problem has been addressed by Clark et al. for the DITE tokamak<sup>29</sup> for the general case where parallel diffusion is sufficiently slow that toroidal asymmetries in the impurity ion distribution can be sustained. We follow their treatment of the problem but restrict our discussion to plasmas where  $T_e \gtrsim 1$  keV and  $Z_{eff} \lesssim 2$  so that over most of the plasma, the impurity ions are relatively collisionless. That is, the collisional mean-free path is  $\gtrsim 2\pi R_{pl} q$  where  $R_{pl}$  is the plasma major radius and  $q$  is the safety factor. This assumption is usually valid for neutral beam heated plasmas on PDX or those expected in TFTR, and it allows us to obtain a simple expression for  $\xi(R)$ .

Ignoring the rotational transform of the field for the moment, we consider a one-dimensional model for the ion motion along the field line. Referring to Fig. 17, we let  $S$  denote the displacement along a field line and, for  $-d < S < d$ , a neutral density from a neutral beam induces charge-exchange



reactions between the beam neutrals and impurity ions with density  $n_2$  to produce particles with density  $n_{Z-1}$ . The length of the field line around the torus is taken to be  $2L$ . Taking ionization and charge-exchange recombination to be the dominant atomic processes (which is easily the case for He, and less valid for O), the continuity equations for particles moving in the +S direction are

$$v \frac{\partial n_{Z-1}}{\partial S} = \frac{n_2}{\tau_{cx}} - \frac{n_{Z-1}}{\tau_i} \quad -d < S < d \quad (27a)$$

$$v \frac{\partial n_{Z-1}}{\partial S} = - \frac{n_{Z-1}}{\tau_i} \quad L > |S| > d \quad (27b)$$

where  $\tau_i = N_e I_{Z-1}$  is the electron impact ionization time and  $\tau_{cx}^{-1} = \sum n_j \langle \sigma v \rangle_j^T$ . For simplicity, we also assume that the ionization distribution is not drastically changed so that we may take the density of fully stripped ions,  $n_2$ , to be constant. Expressing the density as a fraction of the value obtained in equilibrium in the beam region

$$\xi \equiv \frac{n_{Z-1}}{n_2} \frac{\tau_{cx}}{\tau_i}, \quad (28)$$

we use continuity at  $|S| = d$  and  $|S| = L$  to solve for  $\xi$ , which is just the plume attenuation factor of interest. The general solutions are

$$\xi_+(S) = 1 - \frac{\sinh((L-d)/\lambda_i)}{\sinh(L/\lambda_i)} e^{-S/\lambda_i} \quad (29a)$$

for  $d > S > d$ , and

$$\xi_+(S) = \frac{2 \sinh(d/\lambda_i)}{1 - e^{-2L/\lambda_i}} e^{-S/\lambda_i} \quad (29b)$$

for  $L < S < d$ , and

$$\xi_+(S) = \frac{2 \sinh(d/\lambda_i)}{1 - e^{-2L/\lambda_i}} e^{-(2L + S)/\lambda_i} \quad (29c)$$

for  $-d < S < -L$ .

Here  $\lambda_i = v\tau_i$  is the ionization mean-free path for particles with velocity  $v$ . We have taken  $v = (2kT/\pi m)^{1/2}$ , but in the very collisionless case, the  $\xi_+$  could equally well be integrated over a Maxwellian distribution. This only changes the final result by about a factor of 1.5 or so at most. The + subscript on  $\xi$  indicates that we have considered only particles going in the +S direction, and there is an identical population going in the -S direction that must also be included. Putting these results in the context of our experimental situation, we have  $L = \pi Rq$ , while  $S$  represents the arc length around the torus between the neutral beam center and the spectrometer sightline at a given  $R$ , and  $2d$  is the intersection length of a flux tube through the neutral beam at  $R$ .

We consider two limiting cases of practical interest. For very low  $Z$ , such as  $\text{He}^+$ , it is usually true that  $2d \ll \lambda_i \ll L$ . That is, the hydrogenic ions are reionized to the fully stripped state before going once around the torus (hence the term ion plume). Here the negative-going ions never reach the spectrometer line of sight and the plume attenuation factor becomes

$$\xi(S) = \frac{d}{\lambda_i} e^{-S/\lambda_i} \quad (S > d) \quad (30)$$

Then for  $S \ll \lambda_i$  (i.e., for points on the spectrometer sightline near the beam), the plume attenuation factor is just one half the beam width along the flux tube divided by the ionization mean-free path. For higher  $z$  such as oxygen, the limit  $2d \ll L \ll \lambda_i$  is more applicable and we have

$$\xi(S) = \frac{d}{L} \quad (31)$$

which is just a simplified case of the ions being in ionization-charge exchange equilibrium around the torus but with the neutral beam density being the volume averaged neutral density instead of the local beam density. This is just the expected limit for  $\lambda_i \gg L$ .

It is the short  $\lambda_i$  limit that gives the greatest ion plume intensity contribution, and hence the problem in general will be more severe for He than C or O. We note, however, that since  $\lambda_i < \pi R$ , the hydrogenic ions do not circle the torus before ionizing and the spectrometer line-of-sight through the ion plume can be minimized by viewing vertically instead of in the horizontal midplane or, conversely, the beam could inject vertically.

We have calculated the ion plume to prompt charge-exchange intensity ratio given by Eq. (26) for cases of interest on the PDX and TFTR tokamaks to illustrate typical results. A computer code calculates the expression in Eq. (26) using Eqs. (29a-c) as appropriate to account for all intersections of the neutral beam and spectrometer sightline with a given flux surface of major radius  $R$ . Before discussing the results, we note two subtleties of the calculations. The first is that presence of  $\ell$ -mixing in excited states can increase the branching ratio drastically above that with no  $\ell$ -mixing, resulting in a greatly enhanced plume intensity. For example, the HeII 4686 Å (4-3) line is increased by a factor of 7 by the presence of  $\ell$ -mixing when

excited from the ground state by electron impact, as previously mentioned in Sec. II. The second point is that the field lines do in fact have a nonzero rotational transform and, depending on the beam height, spectrometer viewing geometry, and the separation along a flux tube between the beam and spectrometer sightline, the ion plume can rotate around the center of the plasma and not cross the spectrometer sightline at all. This of course assumes that cross field transport within the flux surface is negligible. We account for this in our calculations by assuming  $B_p/B_T \approx a/q(a)R$  for all  $r$  down to some  $r$  near the plasma center, where  $r = R - R_{pl}$  is the minor radius of a given flux surface,  $B_p$  is the poloidal field strength and  $B_T$  is the toroidal field strength. Given this tilt of the magnetic field lines, the contribution to the integral in Eq. (26) at a given  $R$  is set to zero if the vertical separation between the beam center and the spectrometer sightline is greater than one half of the nominal beam height. The assumption of a constant  $B_p/B_T$  down to some cutoff  $r$  is roughly consistent with the rotational transform as a function of  $r$  calculated for several PDX cases using measured  $N_e$  and  $T_e$  profiles as a function of time and solving the magnetic diffusion equation to derive  $B_p(r,t)$ . Although relatively crude, these assumptions allows us to get first order estimates of the plume intensity and spatial distribution. The calculations are most uncertain for the cold plasma edge where the assumption of collisionless parallel transport is no longer valid.

For the sample cases for TFTR and PDX, we set the position of the neutral beam and vary the tangency radius of the spectrometer sightline to scan the intersection region in  $R$ . Parabolic density profiles with the temperature profiles proportional to the square of the density profile are assumed for both cases.  $R_{pl} = 145$  cm,  $a = 40$  cm,  $N_e(0) = 4 \times 10^{13}$  cm<sup>-3</sup>, and  $T_e(0) = 1.5$  keV are used for the PDX example while the TFTR case has  $R_{pl} =$

250 cm,  $a = 80$  cm,  $N_e(0) = 5 \times 10^{13}$  cm<sup>-3</sup>, and  $T_e(0) = 1.5$  keV. The safety factor  $q(a)$  is taken to be 3 for both cases and a full beam height of 16 cm is assumed for PDX and 40 cm for TFTR. The distinguishing feature between the two cases is that the beam injection angle in PDX is near perpendicular with a 35 cm tangency radius while in TFTR the injection is nearly tangential with a tangency radius of 230 cm. The toroidal separation in the plasma midplane between the spectrometer pivot point and the location of the beam source is taken to be 56° in the PDX cases and 78° in TFTR, both values chosen to reflect actual experimental setups. A horizontal beam width of 16 cm is assumed for PDX and 20 cm for TFTR, while a primary beam energy of 22 or 44 keV/amu (44 kV D<sup>0</sup> or H<sup>0</sup>) is used for PDX and 90 keV/amu (H<sup>+</sup>) is assumed for TFTR. For comparison, the 90 keV/amu case is calculated for PDX also. The beam species ratio is assumed to be 2:1:1 for both cases. Charge-exchange rates from Figs. 9-11 are used along with electron impact excitation rates obtained by Mewe<sup>30</sup> and electron ionization rate coefficients from Bell et al.<sup>31</sup> Both the neutral beam and spectrometer are assumed to be in the plasma midplane.

The plume-to-prompt intensity ratio is plotted as a function of the neutral beam-spectrometer sightline intersection radius for these two cases in Figs. 18 and 19 for a few transitions of interest. These results show a few general features that merit mentioning. The drop with beam energy reflects the increase in the charge-exchange excitation rate of these Rydberg transitions as the beam energy increases. In fact, the 90 keV/amu energy assumed for the TFTR case accounts for most of the reduced ratio for He<sup>+</sup> seen in Fig. 19 compared to the He<sup>+</sup> cases in Fig. 18. This is evident from a comparison of the 90 keV/amu case to the lower energy cases in Fig. 18. Likewise, the increase in the ratio when using the  $\Delta n = 10-9$  OVIII transition

instead of the 7-6 OVIII transition is due to the rapid drop in the charge-exchange excitation rate as  $n$  increases.

As expected, the plume/prompt ratio is largest for the  $\text{He}^+$  cases, and often is negligible for the  $\text{O}^{7+}$  transition. When the beam energy is low, only the  $\text{C}^{5+}$  and  $\text{O}^{7+}$  Rydberg transitions will be relatively unpolluted by plume intensity and hence are preferred for ion temperature measurements even though they are in the UV instead of visible spectral regions (the visible Rydberg transitions are not sufficiently excited at low energies). At low beam energies, the  $\text{He}^+$  case can be improved upon by viewing vertically with the spectrometer or neutral beam so that the path length through the drifting ion population is minimized.

When the drifting ion plume intensity is comparable to the prompt charge-exchange signal, it affects the ion velocity distribution measurements only insofar as the plume has nonzero intensity at radii different from the intersection radius so that the source is no longer localized. Examples of the radial distribution of the  $\text{He}^+$  plume intensity ratio are shown in Fig. 20 for the 45 keV/amu case of Fig. 18. In general, the maximum contribution comes from the tangency radius of the spectrometer sightline where the path length through a flux tube is maximized. Depending on the particular experimental setup, this can be quite different from  $R_I$ , the intersection radius. For  $R_I < R_{p\ell}$ , the spatial extent of the plume intensity is quite large and hence more reliable  $T_i$  values can be expected for  $R_I > R_{p\ell}$ . Even then, one should correct the value of  $R$  to which a measured  $T_i$  is assigned by estimating a value weighted by the prompt and plume intensities. It should be noted that the sharp discontinuities in the plume profiles at large  $R$  in Fig. 19 are artifacts in the calculation due to the assumption of a rectangular profile of the beam intensity in the vertical direction. The reduction in

intensity as the magnetic field lines rotate the plume out of the spectrometer sightline thus shows as an abrupt drop instead of a more realistic gradual decrease.

In general, the plume intensity should be checked for each case and geometry of interest, since beam properties, plasma parameters, and experimental conditions all influence the plume/prompt ratio. It is most important for lowest  $Z$  elements such as He and Li, and for the resonant 2-1 transitions for all elements since the electron excitation rate for these transitions is a maximum for a given element. Thus it will be of considerable importance in CXRS measurements of thermalized He ash and in low- $Z$  impurity transport experiments which employ the 2-1 transitions in order to exploit their high intensities under charge-exchange excitation.

#### V. EXPERIMENTAL RESULTS

Observations have been made on the PDX tokamak to illustrate ion velocity distribution measurements using CXRS. A schematic of one of the experimental setups used is shown in Fig. 21. Here, one of the main heating beams is used as the fast neutral source. Each beamline (out of a total of four on PDX) injects near perpendicularly into the torus with a primary beam energy of 40 to 46 kV and total power of 1.0 to 1.5 MW. For these experiments, the neutral beam viewed by the spectrometer (designated by its geographical location on the torus) was not modulated, but since the beams do not overlap, spatially localized measurements are still possible. The beamline has a FWHM of 16 to 20 cm in the plasma center, and a spatial resolution of  $\sim 10$  cm centered on the intersection volume is available when the spectrometer field of view and beam width are taken into account. Both the beamline and spectrometer sightline lie in the plasma midplane.

Light collected by the collimating lens is transmitted by a quartz fiber optic bundle to the remote spectrometer. Only the small collimating telescope with an associated scanner drive is physically near the tokamak. The major radius of the intersection region of the beam and spectrometer sightline was varied on a shot-to-shot basis by rotating the collimating telescope at the window port.

As shown in Fig. 21, a 0.5 m focal length spectrometer with a rapid scanning mirror on the exit slit assembly is used to obtain a short range spectral scan across the line profile every 50 ms. While this system is extremely simple, it has the disadvantage of relatively low efficiency, and an optical multichannel analyzer is preferred for high time resolution with reasonable signal-to-noise ratios.

The measurements reported here were made during a series of runs studying the ASDEX-like high confinement regime (H-mode)<sup>32</sup> in a single null divertor configuration.<sup>33</sup> Typical plasma parameters were  $T_e(0) = 1.5$  to 2.0 keV,  $\bar{n}_e = 1$  to  $4 \times 10^{13}$  cm<sup>-3</sup>,  $I_p = 400$  kA,  $R_p = 140$  cm, and  $a = 40$  cm. The neutral beams were run with either H<sup>0</sup> or D<sup>0</sup>, and the plasma working gas was D<sup>+</sup> except during a short run with a He<sup>++</sup> plasma. Typical total beam power injected was 2 to 3 MW, which required two D<sup>0</sup> or three H<sup>0</sup> beams. Plasma discharge lengths were 900 ms with beam injection for 300 ms.

Spectral profiles of the HeII 4686 line with and without the neutral beams are shown in Fig. 22 for the H<sup>0</sup> D<sup>+</sup> case. A broad component is evident when the EAST beamline is on, and this feature is caused predominantly by charge-exchange excitation of the He<sup>+</sup> in the beam-spectrometer intersection region. The narrow component is due to electron impact excitation of He<sup>+</sup> at the cool plasma periphery and is present even when the neutral beam is off [cf., Fig. 22(a)]. The increased noise level during neutral beam heating is due to instabilities in the plasma edge in H-mode discharges.



The HeII 4686 Å ( $\Delta n = 4$  to 3) line was used for these measurements because the beam energy was usually too low to excite sufficiently the high Rydberg transitions of  $O^{7+}$  and  $C^{5+}$ . With a 45 keV/amu  $H^0$  beam, the  $\Delta n = 10-9$  OVIII transition at 6070 Å was observed during beam injection but with intensities too low for reliable line profile measurements. Some of the low intensity was due to poor sensitivity of the grating above 5500 Å. Helium was present in the plasma in concentrations of a few percent of the electron density, the source being both leakage of He into the discharge from several neutral particle energy analyzers and a small addition of He to the prefill gas.

For the experimental arrangement shown in Fig. 21, only  $H^0$  beams provide useful  $T_i$  measurements because the charge-exchange excitation of HeII 4686 Å is quite weak with 22 keV/amu  $D^0$  beams and a large amount of  $He^{++}$  is required for good signal strength. In addition, the central plume/prompt ratio is estimated to be  $> 1.2$  for the  $D^0$  beam with typical plasma parameters. This ratio is reduced to 0.3 to 0.4 for the  $H^0$  beam, and about half of this plume intensity originates at radii within  $\pm 5$  cm of the intersection radius.

The ion temperature and toroidal rotation velocity are determined from the measured line profiles by using a nonlinear least squares fitting procedure to fit a double gaussian function to the measured profile. A polynomial is included in the fitting function to account for a time varying background intensity. The resulting fits for the data in Fig. 22 are shown by the solid lines. The residual difference between the fitted function and data is shown for each case. The instrumental profile of the spectrometer is roughly gaussian with a FWHM of  $\sim 1$  Å. The width of the broad component gives the ion temperature in the intersection volume while the separation between

the centers of the narrow and broad components gives the toroidal rotation speed with respect to the plasma edge. Uncertainties in the derived values of  $v_\phi$  and  $T_i$  due to both statistical uncertainties in the fits and shot-to-shot variations are included in the final uncertainty estimates. Shot-to-shot variations were dominant for these runs. The transition to the H-mode regime occurred at times in the discharges that varied over a 50 ms range (from 510-560 ms), which further increased the shot-to-shot variations. An estimate of the edge temperature near the separatrix at  $r = 40$  cm is derived from the width of the narrow spectral component.

The resulting ion temperature and rotation velocity profiles for these discharges are shown in Figs. 23 and 24 for three times in the discharge. The error bars shown indicate estimates derived from combining the uncertainties in the fit parameters with uncertainties from shot-to-shot variations obtained from repeated shots with  $R_I = 145$  cm. Central values of  $T_i$  determined by passive charge-exchange measurements of the neutral particle energy spectrum<sup>34</sup> are also indicated. The CXRS and passive charge-exchange values agree within their estimated error bars.

The values of  $T_i$  and  $v_\phi$  rise rapidly during the early phase of neutral injection ( $t \approx 400$  to 450 ms), and small variations in the neutral injector timing and the spectrometer scanner phase can give rise to larger uncertainties in  $T_i(r)$  and  $v_\phi(r)$  at early times. The  $T_i$  and  $v_\phi$  profiles broaden substantially after the transition to the H-mode phase of the discharge, and they indicate sharper gradients near the plasma edge (cf.,  $t = 660$  ms in Fig. 23). This qualitative behavior is characteristic of other plasma properties [e.g.,  $N_e(r)$ ,  $T_e(r)$ ] in H-mode discharges. A residual plume intensity may cause a slight decrease in the measured  $T_i$  near the plasma center, especially during the low  $N_e$  L-mode phase of the discharge (i.e.,  $t =$

510 ns), but should be less important at later times as  $N_e$  and  $T_e$  rise and hence shorten the  $He^+$  ionization path length. The radial resolution in this initial data set is just marginally acceptable and may contribute to the high temperature values at large R, but it can be significantly improved by using a more favorable beam-spectrometer geometry where the spectrometer line-of-sight crosses the beamline near the sightline tangency point. It is clear from these results that time resolved  $T_i$  and  $v_\phi$  radial profiles can be routinely obtained using CXRS.

The existence of a non-gaussian line profile arising from the presence of the drifting ion plume was observed during a series of  $D^0 + He^{++}$  plasma shots. These were most favorable for such observations because the  $He^{++}$  plasma gives a very high intensity signal while the 21 keV/amu  $D^0$  beams gave a high plume/prompt ratio (cf., Fig. 18). Figure 25(a) shows a HeII 4686 Å line profile ( $R_I = 140$  cm) when the EAST beam was off, and hence the broad component is due to the two other neutral beams (including SOUTH in Fig. 21) which were on. The resulting fit to a double gaussian profile shows that the wings of the line are poorly modeled, suggesting that radiation from several radii are significantly contributing to the observed emission. A similar result is obtained in this case when only the EAST beam itself is on, but here the direct charge-exchange signal also contributes and tends to reduce the non-gaussian component. This is seen in Fig. 25(b), where again the line profile wing is not well-matched by the assumed gaussian profiles. This broad component in the wings of the line when the EAST beam is off was hardly evident in the  $H^0 + D^0$  cases plotted in Figs. 23 and 24, reflecting primarily the advantage of using higher energy beams to reduce the relative intensity due to drifting ions and, to a lesser degree, more favorable plasma profiles in these  $H^0 + D^+$  discharges.

Judicious choice of beam-spectrometer geometry allows reasonably accurate  $T_i(r,t)$  measurements even with the low energy  $D^0$  beams. The experimental arrangement on PDX was modified to reflect the arrangement shown in Fig. 16, where the sightline crosses the neutral beam almost at the tangency radius of the sightline. This reduces the radial delocalization due to the ion plume, as indicated in Fig. 20 (the shape of the plume intensity radial distribution is rather insensitive to the neutral beam energy). To reduce any influence from other neutral beams, the NORTHWEST beam on PDX was used since this beamline is toroidally separated from all others by at least  $90^\circ$  in either direction. (Modulation of the beam as a means of separating the influence of various beamlines was not available for these experiments.) In addition, an optical multichannel analyzer with an intensified photodiode array (Princeton Applied Research Corporation, Model 1420) was installed to provide spectral line profiles every 20 ms with acceptable signal strength.

A plot of the time evolution of ion temperature radial profiles measured with this system is shown in Fig. 26 for  $D^0 + D^+$  circular discharges run while testing a particle scoop limiter on PDX.<sup>35</sup> These plasmas were run at densities of  $\bar{N}_e = 4$  to  $4.5 \times 10^{13} \text{ cm}^{-3}$  which resulted in decreasing the  $\text{He}^+$  ionization mean-free path and hence contributed to decreasing the plume ion intensity, especially from the other beamlines. Reasonable agreement between these results at  $r = 0$  ( $R_i = 155 \text{ cm}$ ) and passive charge exchange was again obtained, and a preliminary analysis of the energy balance for these discharges (using the PPPL TRANSP code<sup>15,36</sup>) indicates that the measured  $T_i$  profiles agree to within 20% with those calculated assuming neoclassical ion thermal conductivity. These results are shown mainly to emphasize the wealth of information available using CXRS with just a few plasma shots. A detailed transport and power balance analysis of these discharges using the above

results along with other information on the plasma properties will be reported elsewhere.

## VI. CONCLUSION

Charge Exchange Recombination Spectroscopy clearly provides a powerful tool for determining the ion velocity distribution in hot plasmas. Ion temperature profiles can be obtained with good spatial resolution using the relatively benign low-Z impurities that are present in most fusion plasma experiments. With high beam energies and/or reasonable access for the neutral beam-spectrometer arrangement, simple fiber optically coupled spectrometer systems are feasible, allowing easy access to reactor environments.

The present discussion has considerably expanded our earlier work,<sup>2</sup> and a number of general observations can be made. Plasma effects, especially ion-ion collisions, can mix different  $l$ -levels and cause substantial changes in expected line intensities. This results in transitions between lower  $n$ -levels of the hydrogenic ions being the most useful for impurity ion density measurements, and it also can cause an increase in the intensity of the transitions between higher Rydberg states. In addition,  $l$ -mixing effects can raise the expected intensities of background radiation caused by electron impact excitation of the hydrogenic ions.

The effects of apparent line broadening due to atomic fine structure must be evaluated and can change depending on excitation processes. This is especially true when velocity distributions are being studied in detail. For overall ion temperature measurements, a correction to the measured temperature can be applied to obtain the actual ion temperature with a high degree of confidence.

The ions produced by the neutral beam which then drift along magnetic field lines into the spectrometer line of sight and are excited by electron collisions can significantly distort ion temperature and fully stripped ion density measurements. This effect is strongest in very low-Z elements because of the low charge-exchange cross sections and high electron excitation rates, but may also cause difficulties for interpreting the intensity of  $\Delta n = 2-1$  transitions in the higher-Z elements such as C and O. It is important to recognize that this effect is independent of beam power and is not avoided by neutral beam modulation unless the beam modulation time is less than the transit time of the ions along the field lines. This ion plume intensity can be especially interfering when trying to measure nonthermal ion distributions in  $\text{He}^{++}$  or other elements because it can lead to nongaussian line profiles due to loss of radial localization of the measurement rather than to any real nonthermal effects.

A very simplified model for calculating the ion plume intensity has been introduced in the foregoing discussion. The use of a one-dimensional model which assumes collisionless ion parallel transport along the field lines, no significant change in the ionization balance due to charge-exchange recombination, and only charge-exchange recombination and electron impact ionization, is not rigorously applicable across the entire plasma cross section. For the case where the ionization path length is greater than the plasma circumference (e.g., for  $\text{C}^{5+}$  and  $\text{O}^{7+}$ ), the model calculations are best considered to be more estimates than quantitative assessments of the pollution of the prompt charge-exchange signal by excitation of drifting ions. However, it is quite clear from both our simple calculations and our experimental results at low beam energies with unfavorable beam-spectrometer access that the ion plume intensity has to be considered carefully for each experimental

situation. The model used here represents a useful first step for such evaluations.

Ion temperature and plasma bulk motion velocities can be measured in most magnetically confined plasma experiments using CXRS. While not necessary, modulation of the neutral beam power is highly desirable to prevent pollution from other beams and to help discriminate against radiation from the cool plasma edge. Visible spectral lines are most attractive for these measurements due to ease of optical access and spectral analysis, but these are best excited only at higher beam energies. For helium and other very light impurities, a vertical viewing geometry is necessary for the most accurate  $T_i$  measurements even though rotation velocity measurements may be sacrificed. If constrained to low energy ( $< 30$  keV/amu) neutral beams and a midplane viewing geometry, use of the ultraviolet lines of  $C^{5+}$  and  $O^{7+}$  will give the most reliable measurements, but fine structure corrections must be made, especially at low temperatures. This approach is planned for the PBX experiment (a modification of the PDX tokamak).

The goal of reliable and relatively simple time- and space-resolved ion velocity distribution measurements seems readily attainable using CXRS provided attention is paid to the various complications we have discussed. While our discussion has concentrated on ion temperature measurements using He, C, or O in tokamak devices, it is easily expanded to other elements and magnetic confinement geometries. In addition, the considerations of intensities, fine structure, and product ion effects obviously are relevant to other applications of CXRS beyond that of ion temperature and plasma rotation measurements.

## ACKNOWLEDGMENTS

The authors wish to thank especially R. Hulse for several seminal suggestions during this work and a critical reading of the manuscript. Useful conversations with D. Post, E. Hinno, R. Goldston, D. Mueller, H. Kugel, and R. Isler are gratefully acknowledged. B. Bransden, R. Olsen, T. Green, E. Shipsey, and J. Browne provided us with several preprints of their calculations of theoretical cross sections. Likewise, R. Isler and R. Groebner graciously provided us with preprints of their work with CXRS on the ISX-B and DIII tokamaks, respectively. P. Roney helped with much of the necessary software for data acquisition and analysis, and H. Towner provided indispensable aid in the neutral beam attenuation calculations.

This work was supported by the U.S. Department of Energy, Contract No. DE-AC02-76-CHO-3073.



## REFERENCES

- <sup>1</sup>Equipe TFR, Nucl. Fusion 18, 647 (1978).
- <sup>2</sup>R.J. Fonck, R.J. Goldston, R. Kaita, and D. Post, Appl. Phys. Lett. 42, 239 (1983).
- <sup>3</sup>H. Eubank *et al.*, in Plasma Physics and Controlled Nuclear Fusion Research, Vol. I, Proceedings of the 7th International Conference, Innsbruck, 1978 (IAEA, Vienna, 1979), p. 167.
- <sup>4</sup>S. Suckewer, H.P. Eubank, R.J. Goldston, J. McEnerney, N.R. Sauthoff, and H.H. Towner, Nucl. Fusion 21, 1301 (1981).
- <sup>5</sup>D.E. Post, D.R. Mikkelsen, R.A. Hulse, L.D. Stewart, and J.C. Weisheit, J. Fusion Energy 1, 129 (1981).
- <sup>6</sup>R.C. Isler and L.E. Murray, Appl. Phys. Lett. 42, 355 (1983).
- <sup>7</sup>A.N. Zimovév, A.A. Korotko, E.R. Krzhizhanovskii, V.V. Afrosimov, and Yu S. Gordeev, Pis'ma Zh. Eksp. Teor. Fiz. 32, 557 (1980) [JETP Lett. 32, 539 (1980)].
- <sup>8</sup>R.J. Fonck, M. Finkenthal, R.J. Goldston, D.L. Herndon, R.A. Hulse, R. Kaita, and D.D. Meyerhofer, Phys. Rev. Lett. 49, 737 (1982).
- <sup>9</sup>R.C. Isler, L.E. Murray, S. Kasai, J.L. Dunlop, S.C. Bates, P.H. Edmonds, E.A. Lazarus, C.H. Ma, and M.M. Murakami, Phys. Rev. A 24, 2701 (1981).
- <sup>10</sup>D.E. Post, L.R. Grisham, and R.J. Fonck, Physica Scr. T3, 135 (1983).
- <sup>11</sup>H. Winter, Comm. on Atomic and Molec. Phys. 12, 165 (1982).
- <sup>12</sup>R.J. Fonck and D.S. Darrow, Bull. Am. Phys. Soc. 28, 939 (1983).
- <sup>13</sup>R.C. Isler, R.A. Langley, and L.E. Murray, Bull. Am. Phys. Soc. 28, 941 (1983).
- <sup>14</sup>R. Groebner, N. Brooks, K. Burrell, L. Rottler, and P. Thomas, Bull. Am. Phys. Soc. 28, 940 (1983); and R.J. Groebner, N. Brooks, K. Burrell, L. Rottler, GA Technologies Report GA-A17145, 1983.

- <sup>15</sup>R.J. Goldston, D.C. McCune, H.H. Towner, S.L. Davis, R.J. Hawryluk, and G.L. Schmidt, *J. Comput. Phys.* 43, 61 (1981).
- <sup>16</sup>R.E. Olsen in Electronic and Atomic Collisions, N. Oda and K. Takayunagi, Eds., 390 (North Holland, Amsterdam, 1980).
- <sup>17</sup>R.E. Olsen, *Phys. Rev. A* 24, 1726 (1981).
- <sup>18</sup>T.A. Green, E.J. Shipsey, and J.C. Browne, *Phys. Rev. A* 25, 1364 (1982).
- <sup>19</sup>E.J. Shipsey, T.A. Green, and J.C. Browne, *Phys. Rev. A* 27, 821 (1983).
- <sup>20</sup>H. Ryufuku and T. Watanabe, *Phys. Rev. A* 18, 2005 (1978).
- <sup>21</sup>H. Ryufuku, Japan Atomic Energy Research Institute Report JAERI 82-031, 1982.
- <sup>22</sup>M. Rosenbluh, P. Pancok, B. Lax, and T.A. Miller, *Phys. Rev. A* 18, 1103 (1978).
- <sup>23</sup>R.M. Pengelly and M.J. Seaton, *MNRAS* 127, 165 (1964).
- <sup>24</sup>H.A. Bethe and E.E. Salpeter, Quantum Mechanics of One- and Two-Electron Atoms (Plenum, New York, 1977) Sec. 17.
- <sup>25</sup>*Ibid*, Sec. 55.
- <sup>26</sup>N.P. Economou, R.R. Freeman, and P.F. Liao, *Phys. Rev. A* 18, 2506 (1978).
- <sup>27</sup>J.D. Garcia and J.E. Mack, *J. Opt. Soc. Am.* 55, 654 (1965).
- <sup>28</sup>H.G. Kuhn, Atomic Spectra, 171 (Academic Press, New York, 1969).
- <sup>29</sup>W.H.M. Clark *et al.*, *Nucl. Fusion* 22, 333 (1982).
- <sup>30</sup>R. Mewe, *Astron. Astrophys.* 20, 215 (1972).
- <sup>31</sup>K.L. Bell, H.B. Gilbody, J.G. Hughes, A.E. Kingston, and F.J. Smith, Culham Laboratory Report CLM-R216 (1981).
- <sup>32</sup>F. Wagner *et al.*, *Phys. Rev. Lett.* 49 1408 (1982).
- <sup>33</sup>S.M. Kaye, *et al.*, *J. Nucl. Materials* (to be published).
- <sup>34</sup>S.L. Davis, D. Mueller, and C.J. Keane, *Rev. Sci. Instrum.* 54, 315 (1983).
- <sup>35</sup>R. Budny *et al.*, *J. Nucl. Materials* (to be published).
- <sup>36</sup>R.J. Hawryluk, in Proceedings of the Course on Physics of Plasma Close to Thermonuclear Conditions, Report EUR-FU-RU/XXII/476/80, Vol. I, p. 19.

## FIGURE CAPTIONS

- FIG. 1 Schematic of cross sections of interest for  $H^{\circ} + C^{6+} + H^{+} + C^{5+}(n,l)$  at 25 keV/amu with the direct charge exchange cross sections taken from Ref. 18. (a) Cross section for populating each level  $(n,l)$  directly via charge exchange; (b) Cascade-corrected total cross sections for populating each  $(n,l)$  level; (c) Total effective cross section for excitation of an  $n+m$  transition.
- FIG. 2 Rate coefficients for excitation of principal  $\Delta n = 1$  transitions in  $He^{+}$  via charge-exchange recombination. Unified distorted wave cross sections from Ref. 21 are used. The wavelength for each transition is given in parentheses.
- FIG. 3 Excitation rate coefficients for  $\Delta n = 1$  transitions in  $C^{5+}$  using the perturbed stationary state cross sections from Ref. 18.
- FIG. 4 Excitation rate coefficients for  $\Delta n = 1$  transitions in  $C^{5+}$  using the unified distorted wave cross sections from Ref. 21. The wavelength for each transition is given in parentheses.
- FIG. 5 Excitation rate coefficients for  $\Delta n = 1$  transitions in  $O^{7+}$  using the perturbed stationary state cross sections from Ref. 19.
- FIG. 6 Excitation rate coefficients for  $\Delta n = 1$  transitions in  $O^{7+}$  using the UDWA cross sections of Ref. 21. The wavelength for each transition is given in parentheses.

- FIG. 7 Critical  $n$ -value for onset of  $l$ -mixing due to ion-ion collisions.  $T_i$  is in keV and  $N_e$  in units of  $10^{13} \text{ cm}^{-3}$ .
- FIG. 8 Approximate  $n$ -value for onset of  $l$ -mixing due to motional Stark effect. Curves for both the linear and quadratic Stark effect estimates are shown.  $T_i$  is in keV and  $B$  in Teslas.
- FIG. 9 Excitation rate coefficients for  $\Delta n = 1$  transitions in  $\text{He}^+$  excited by charge exchange. The UDWA cross sections of Ref. 21 are used and full  $l$ -mixing is assumed for  $n > 2$ .
- FIG. 10 Excitation rate coefficients for  $\Delta n = 1$  transitions in  $\text{C}^{5+}$  with  $l$ -mixing for  $n > 5$ . UDWA cross sections of Ref. 21 are used.
- FIG. 11 Excitation rate coefficients for  $\Delta n = 1$  transitions of  $\text{O}^{7+}$  with  $l$ -mixing for  $n > 6$ . UDWA cross sections of Ref. 21 are used.
- FIG. 12 Fine structure influence on Doppler broadened line profiles. (a)  $\text{He}^+$   $\Delta n = 4-3$  field-free fine structure components; (b) same as (a) with Doppler broadened profiles at  $T_i = 100 \text{ eV}$ ; (c)  $\text{O}^{7+}$   $\Delta n = 6-5$  field-free fine structure; (d) same as (c) with  $T_i = 400 \text{ eV}$ .
- FIG. 13 Ion temperature correction factors due to field-free fine structure for  $\text{He}^+$  with excitation by neutral hydrogen. Complete  $l$ -mixing is assumed for  $n > 2$ . The abscissa is the value of the real ion temperature, not the apparent value.

- FIG. 14 Ion temperature correction factors due to fine structure for  $C^{5+}$  with excitation by 25 keV/amu neutral hydrogen. Complete  $l$ -mixing is assumed for  $n > 5$ .
- FIG. 15 Ion temperature correction factors due to fine structure for  $O^{7+}$  with excitation by 25 keV/amu neutral hydrogen. Complete  $l$ -mixing is assumed for  $n > 6$ .
- FIG. 16 Typical experimental geometry for CXRS measurements on the PDX tokamak. Both the neutral beam and the spectrometer line-of-sight are in the plasma horizontal midplane.
- FIG. 17 One-dimensional geometry for drifting ion plume calculations. (a) Neutral beam density as a function of distance along the field line; (b) Relative density of recombined ions moving in the + direction for  $L = 3\lambda_1 = 9d$ ; (c) Relative density of recombined ions for  $\lambda_1 \gg L$ .
- FIG. 18 Plume/prompt intensity ratios for the PDX geometry with near perpendicular beam injection ( $R_{BT} = 35$  cm,  $R_{Pl} \approx 140$  cm,  $a = 40$  cm).
- FIG. 19 Plume/prompt intensity ratios for the TFTR geometry with tangential injection ( $R_{BT} = 230$  cm,  $R_{Pl} = 250$  cm,  $a = 80$  cm).

FIG. 20 Plume/prompt intensity ratio distribution as a function of major radius for the PDV case with 45 keV/amu hydrogen excitation of  $\text{He}^+$  4686 Å ( $\Delta n = 4-3$ ).  $R_{ST}$  is the tangency radius of the spectrometer sightline while  $R_I$  is the beamline-spectrometer sightline intersection radius.  $R_{pk} = 140$  cm and  $a = 40$  cm.

FIG. 21 Schematic of experimental setup on PDX for CXRS measurements.

FIG. 22 Spectral line profiles of  $\text{He}^+$  4686 Å line from PDX ( $\text{H}^0 + \text{D}^+$ ). (a) Neutral beam off with data fitted to a single gaussian profile (solid line) with a linear background; (b) neutral beam on with data fitted to a sum of two gaussians (solid line) and a linear background. The residual differences between the data and the fitted functions are shown below each data sample. A change in time is equivalent to a linear change in wavelength.

FIG. 23 Radial profiles of ion temperature for  $\text{H}^0 + \text{D}^+$  PDX plasma at three times during the discharge. Closed circles = CXRS measurements; open circles = passive charge exchange results. Beam injection from  $t = 400$  to 700 ms with  $P_{ABS} = 1.5$  to 2.0 MW. Transition to the H-mode occurred between 520 to 550 ms for all shots. Separatrix is at  $R = 180$  cm while the plasma magnetic axis is at  $R = 146$  cm.

FIG. 24 Toroidal rotation speed radial profiles for the same conditions as in Fig. 23. All values of  $v_\phi$  are measured relative to the value at the plasma edge ( $R \approx 180$  cm).

FIG. 25 Nongaussian line profiles at  $4686 \text{ \AA}$  due to recombined ions drifting into the spectrometer line-of-sight.  $D^{\circ} \rightarrow He^{++}$  with geometry as shown in Fig. 21. (a) Line profile with EAST beam off and SOUTH and SOUTHWEST beams on; (b) Line profile with only the EAST beam on. Solid lines are least squares fitted gaussians with fit residuals shown below each line profile.

FIG. 26 Time evolution of ion temperature profile for the  $D^{\circ} \rightarrow D^{+}$  case in PDX with the geometry of Fig. 16. Scoop limited discharges with  $P_{ABS} \approx 2.3 \text{ MW}$ ,  $R_{pl} = 153 \text{ cm}$ , and  $a = 40 \text{ cm}$ . Each intersection point on the grid surface represents a datum. The neutral beam was on from 300 to 600 ms.

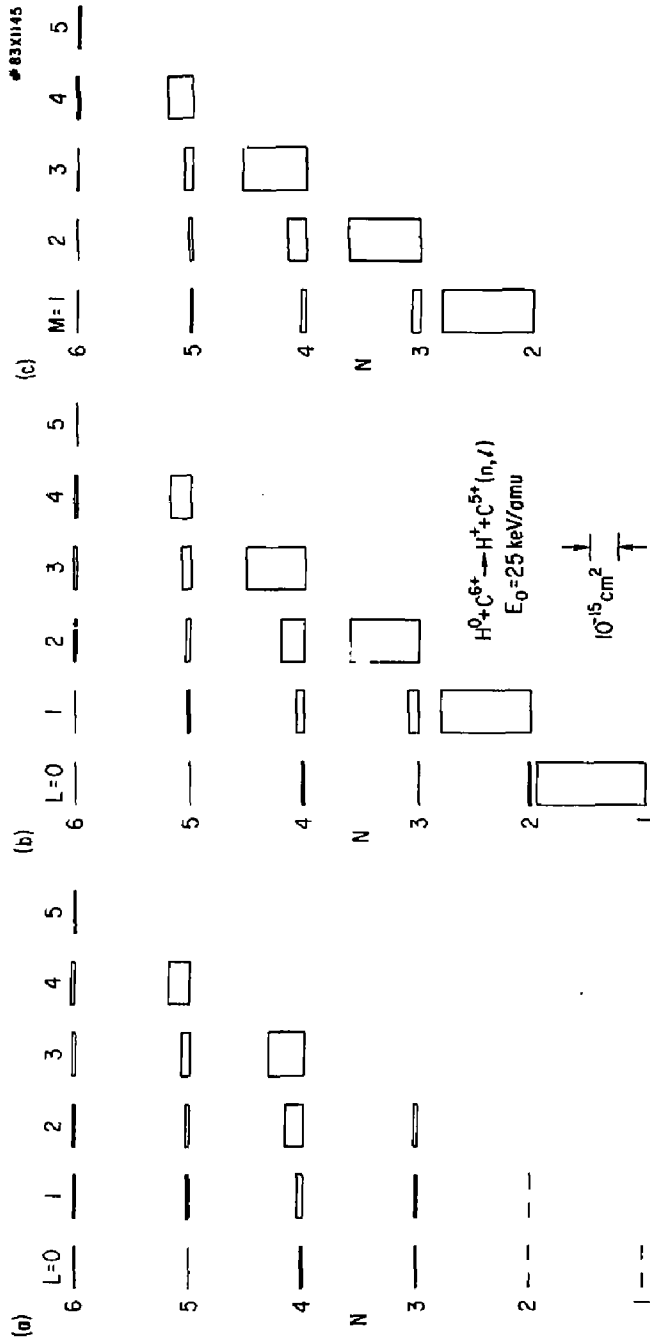


Fig. 1



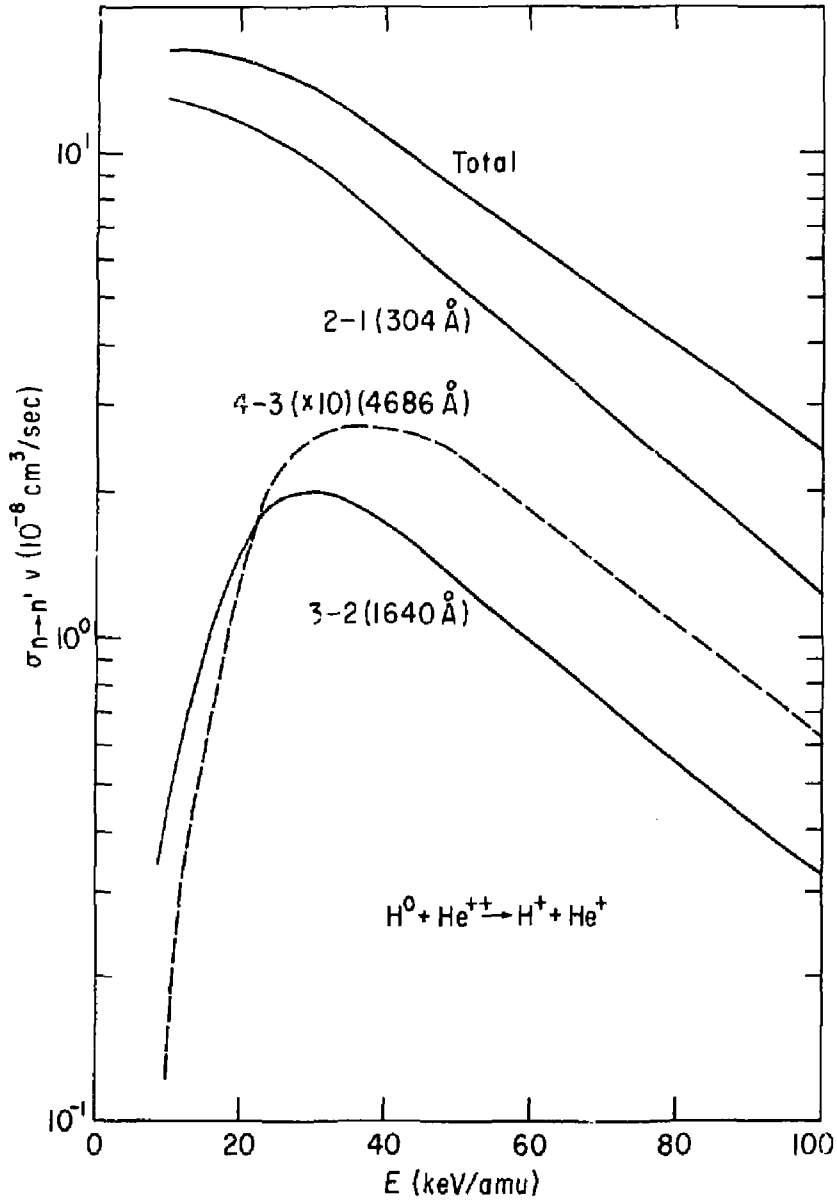


Fig. 2

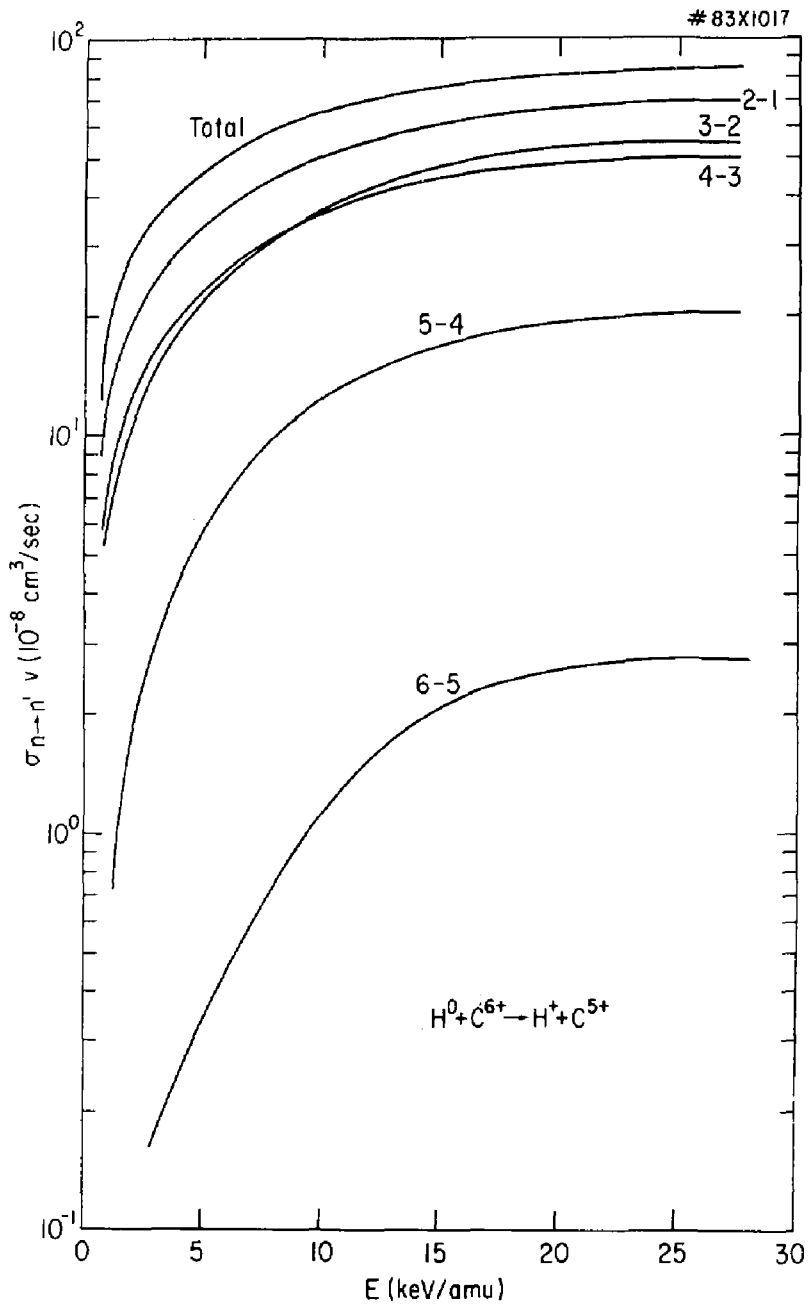


Fig. 3

#83X1022

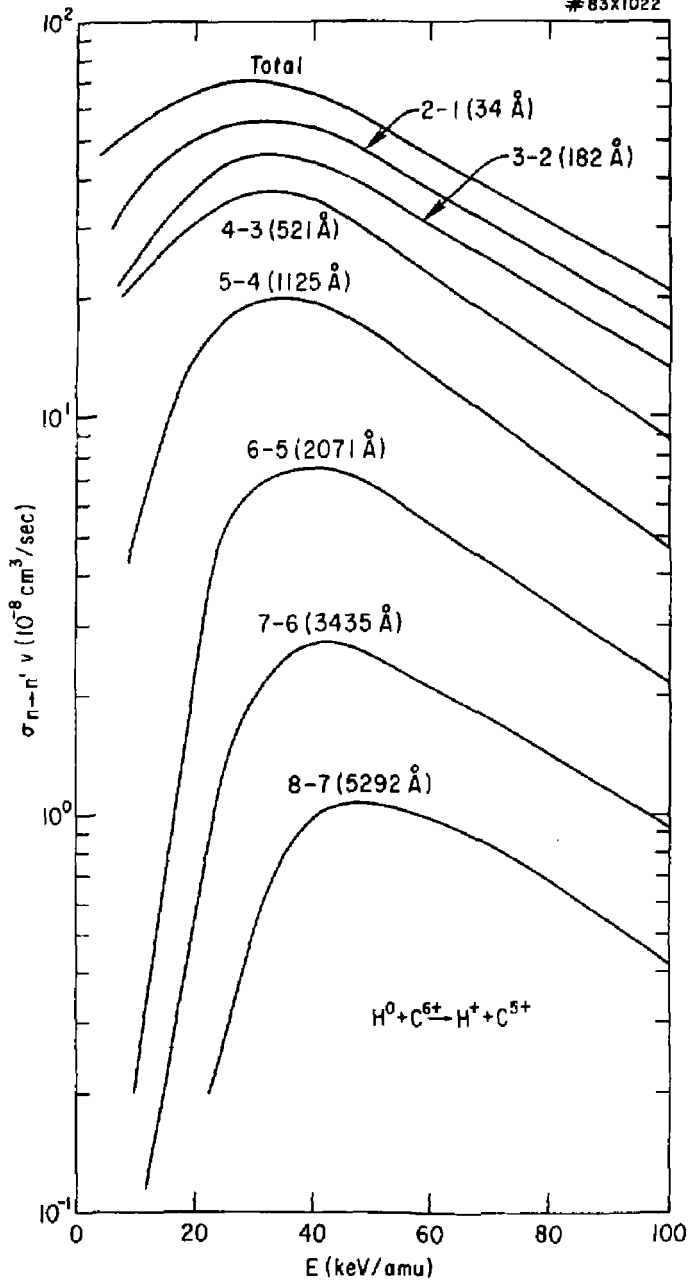


Fig. 4

# 83X1226

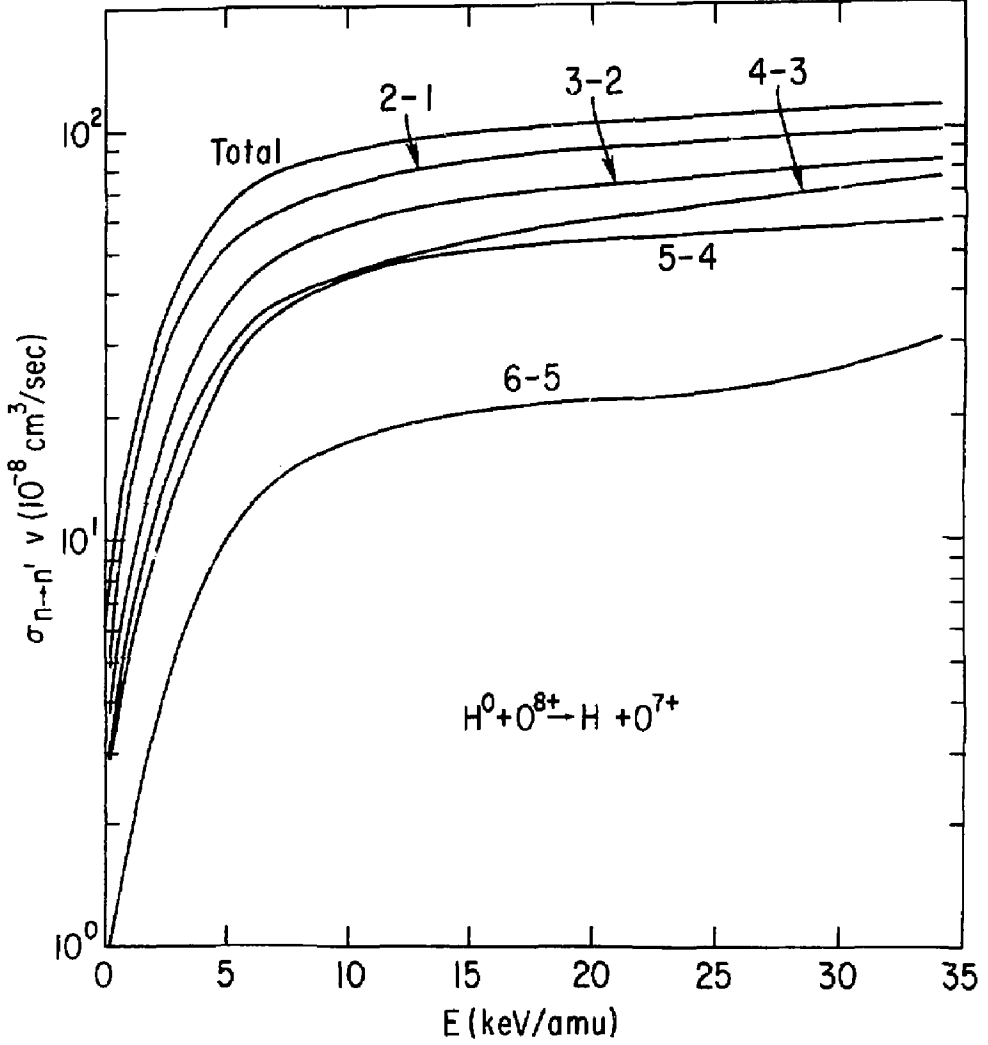


Fig. 5

# 83X1019

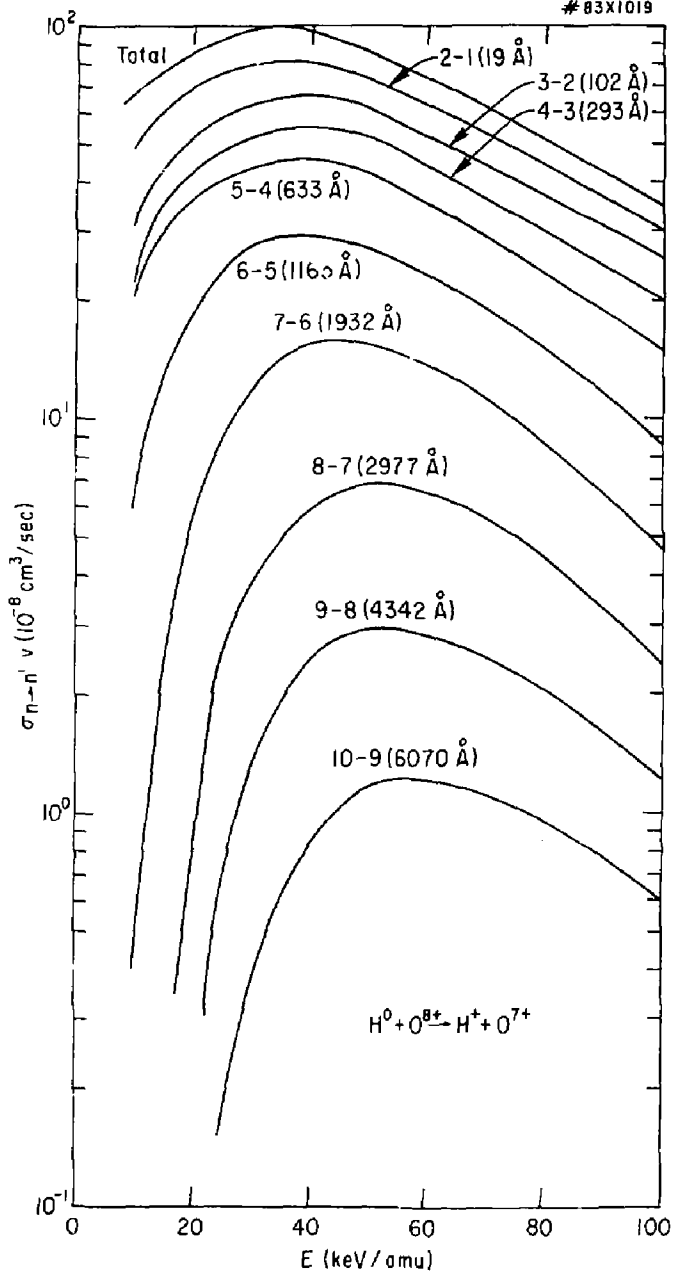


Fig. 6

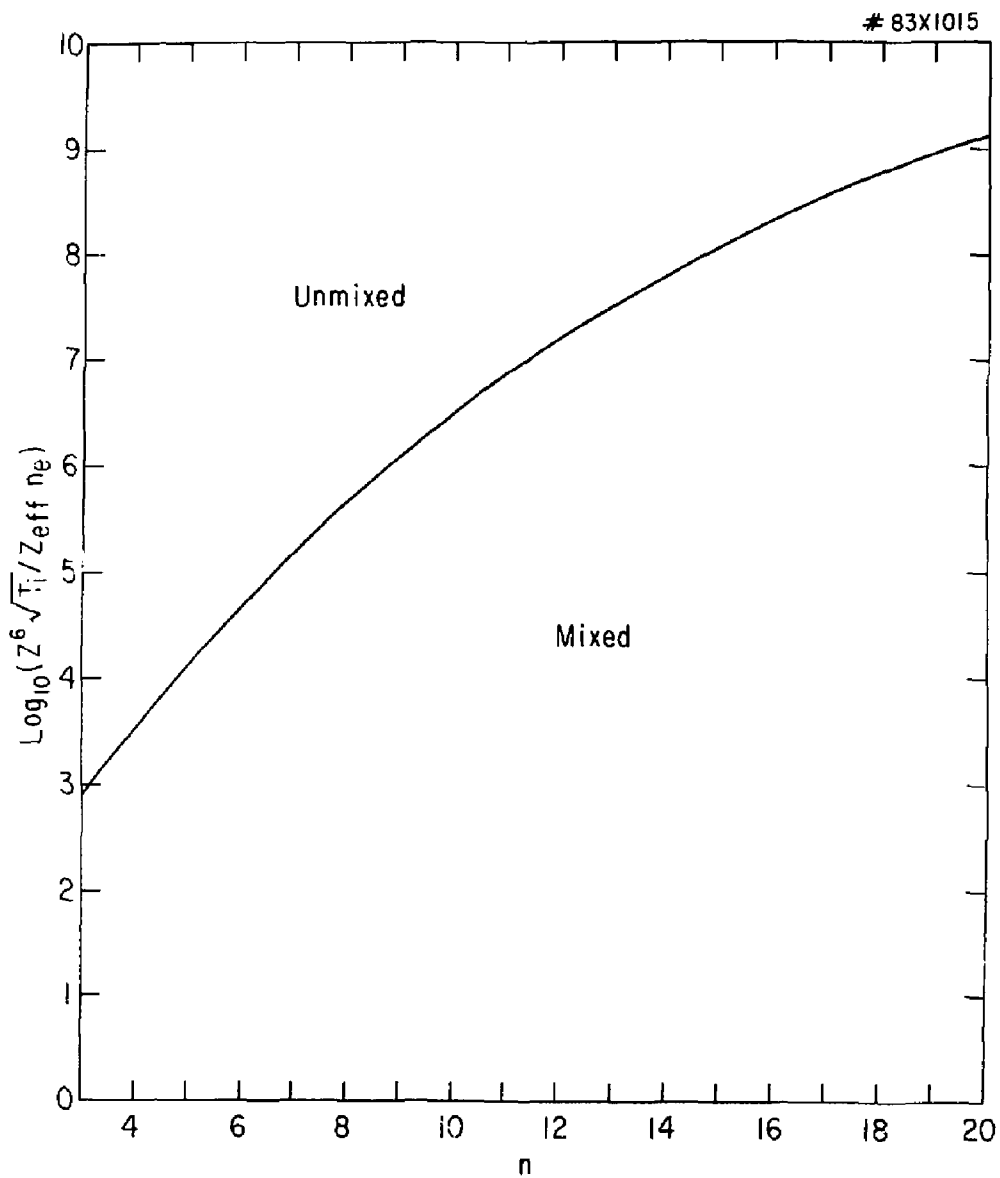


Fig. 7

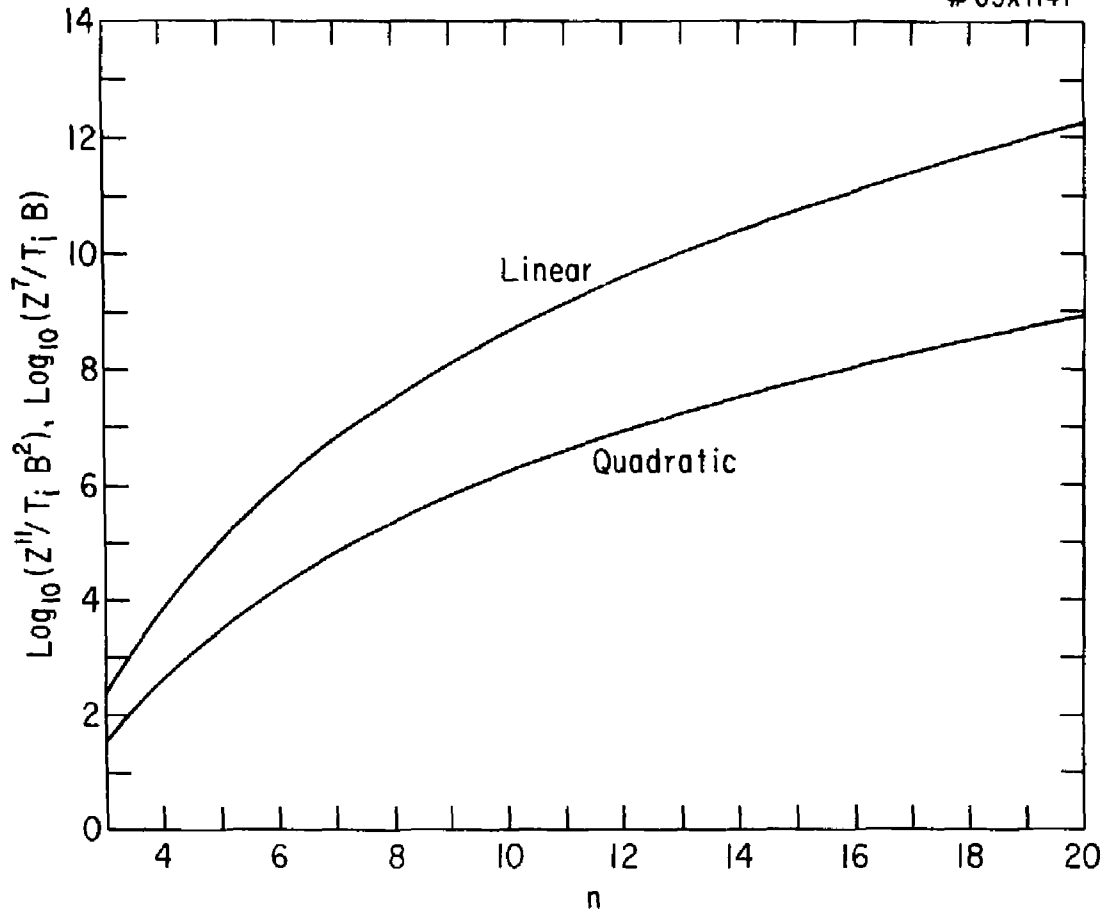


Fig. 8

#84X0099

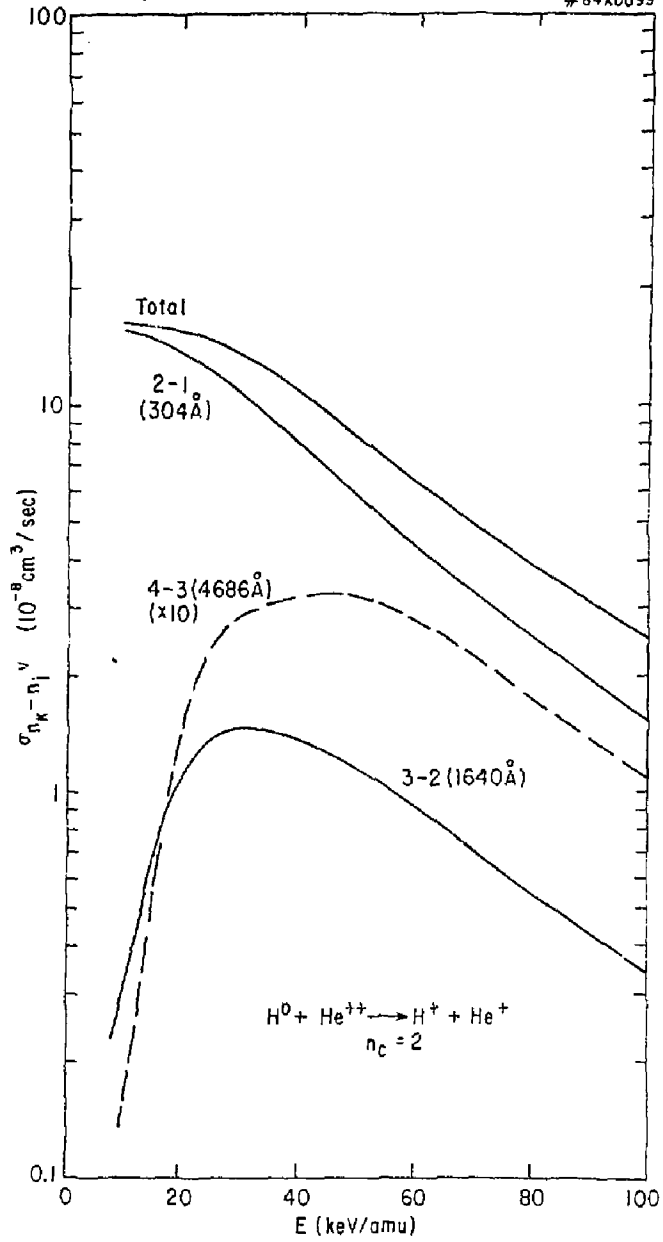


Fig. 9



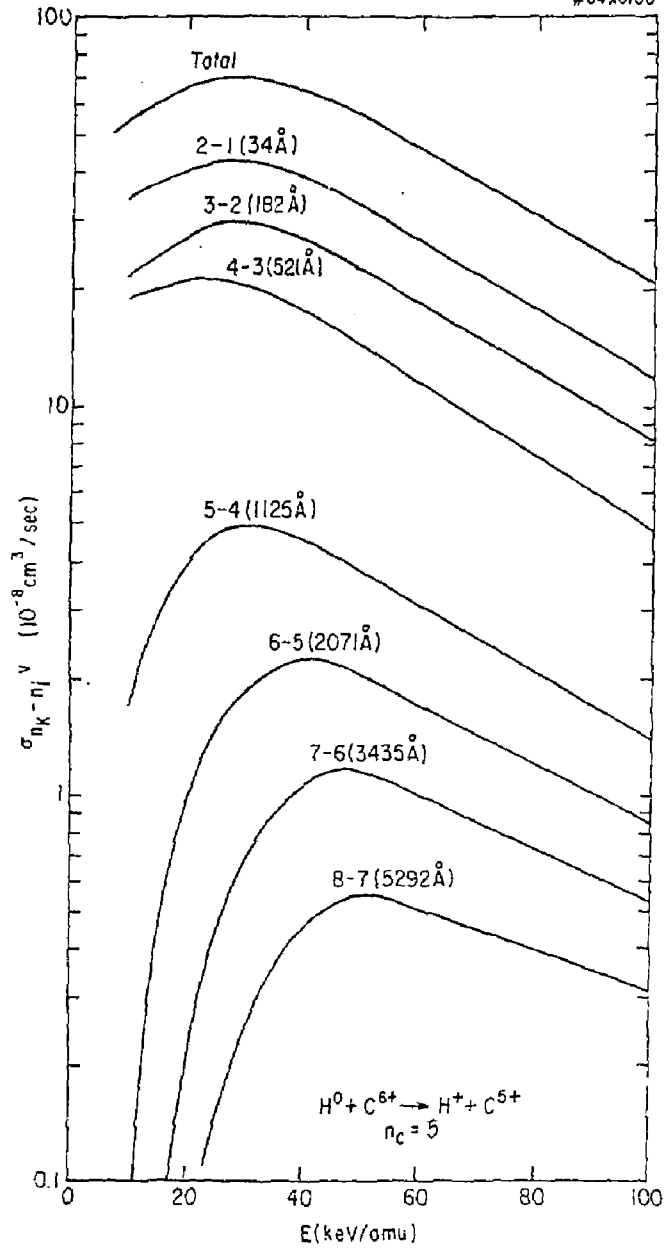


Fig. 10

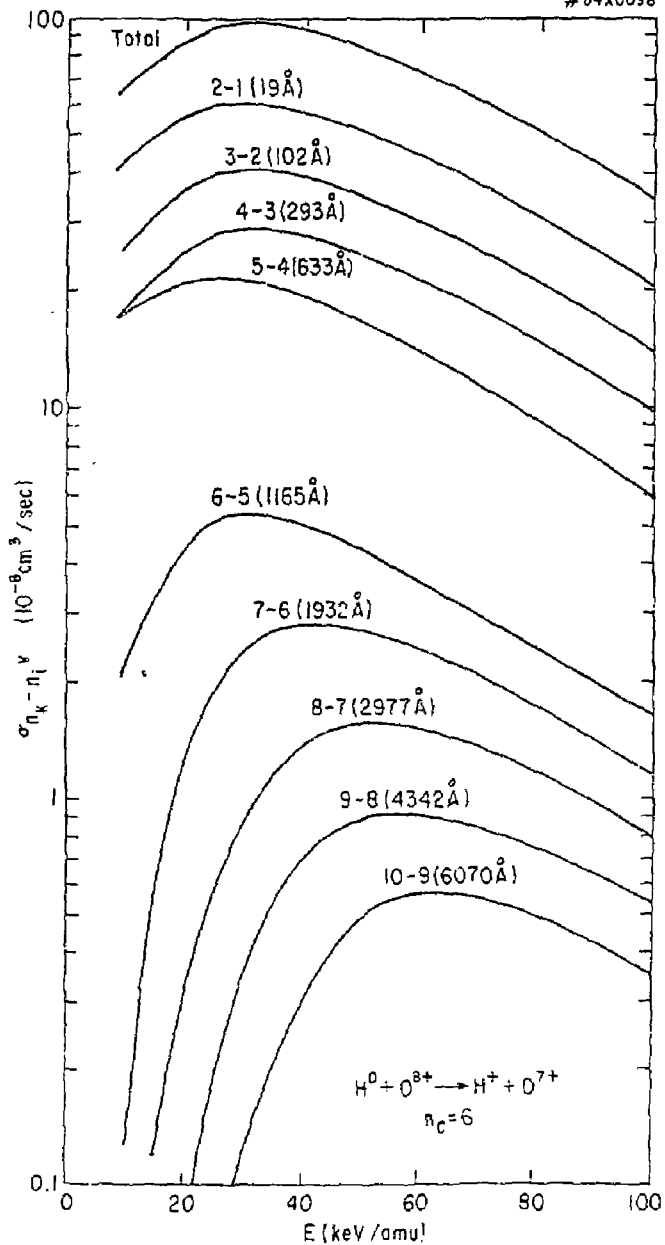


Fig. 11

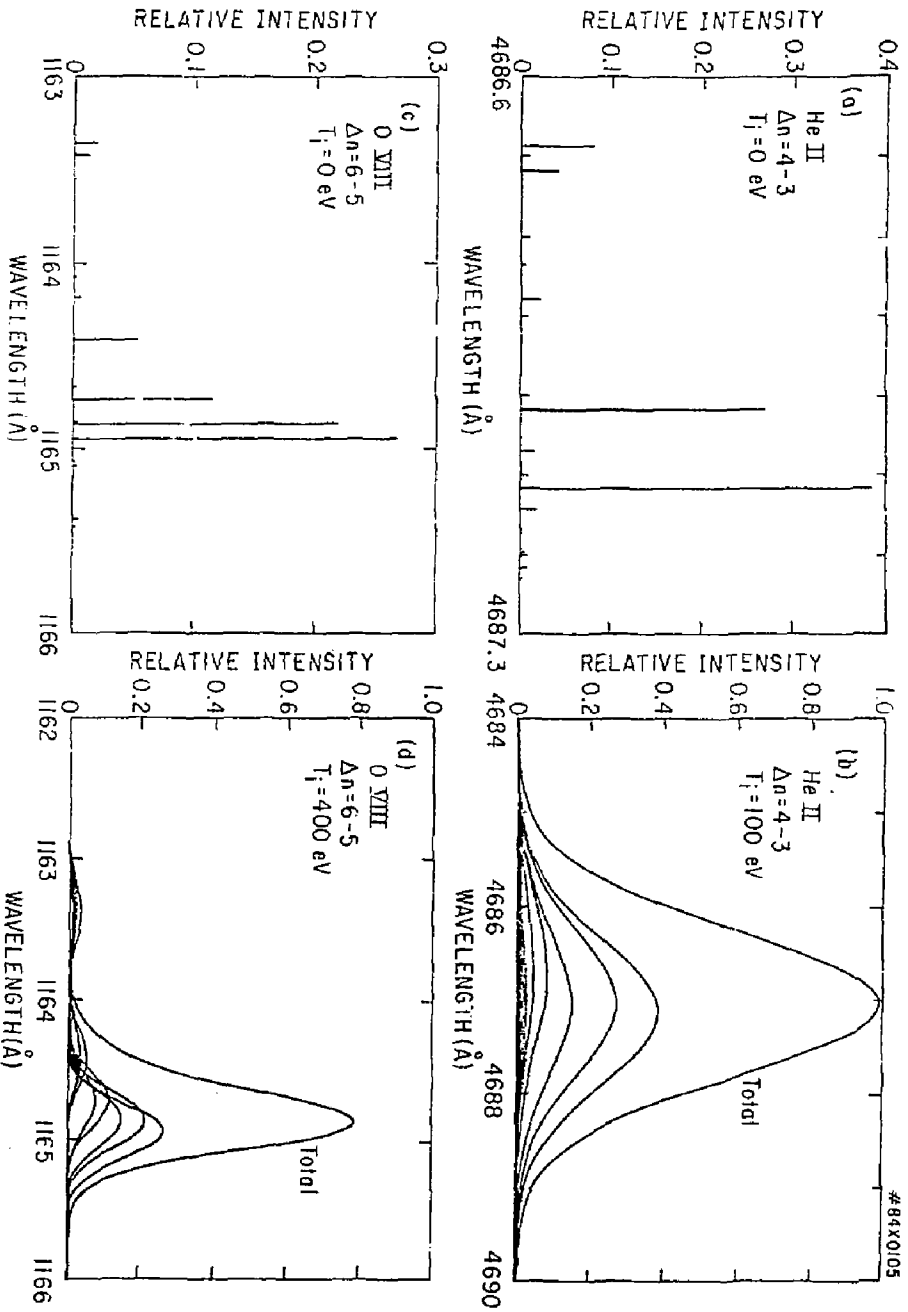


Fig. 12

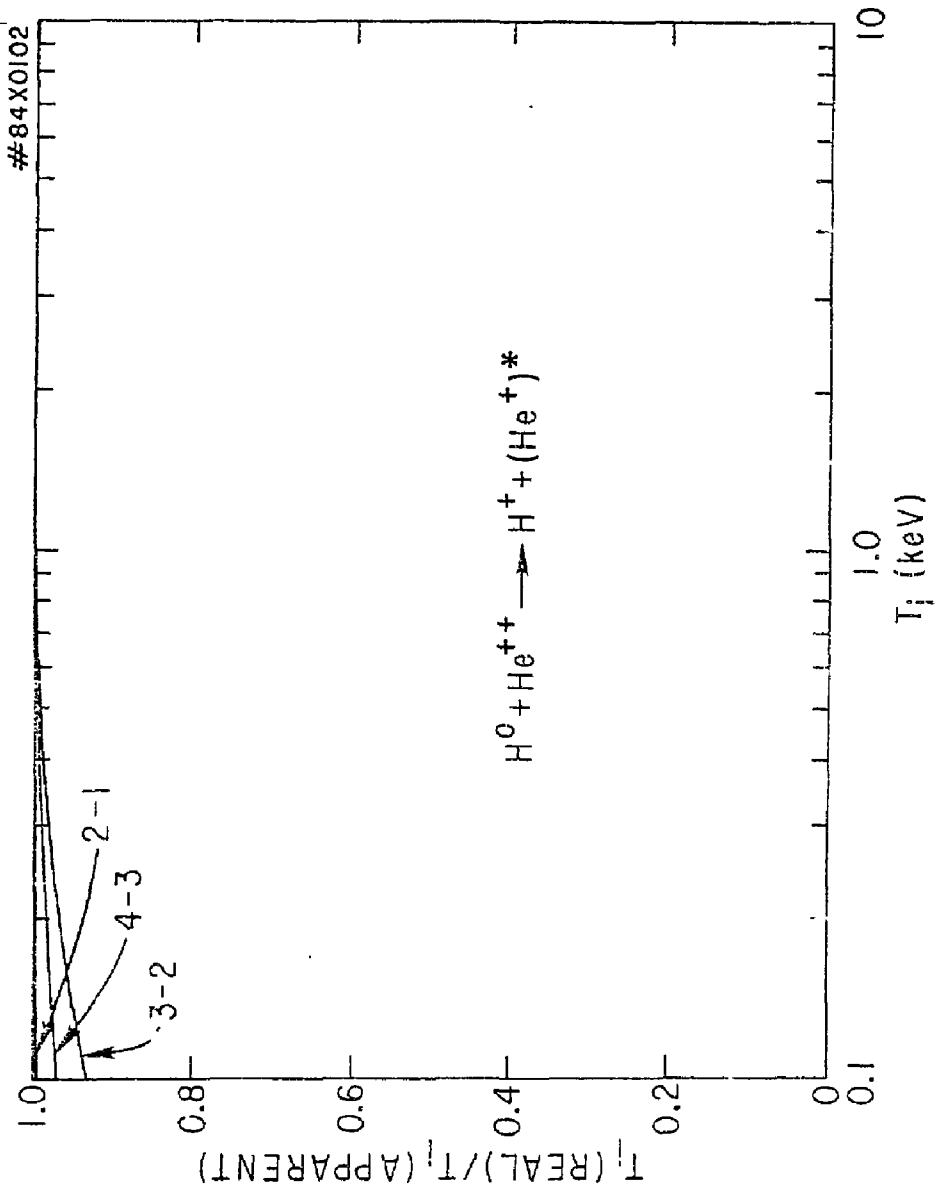


FIG. 13

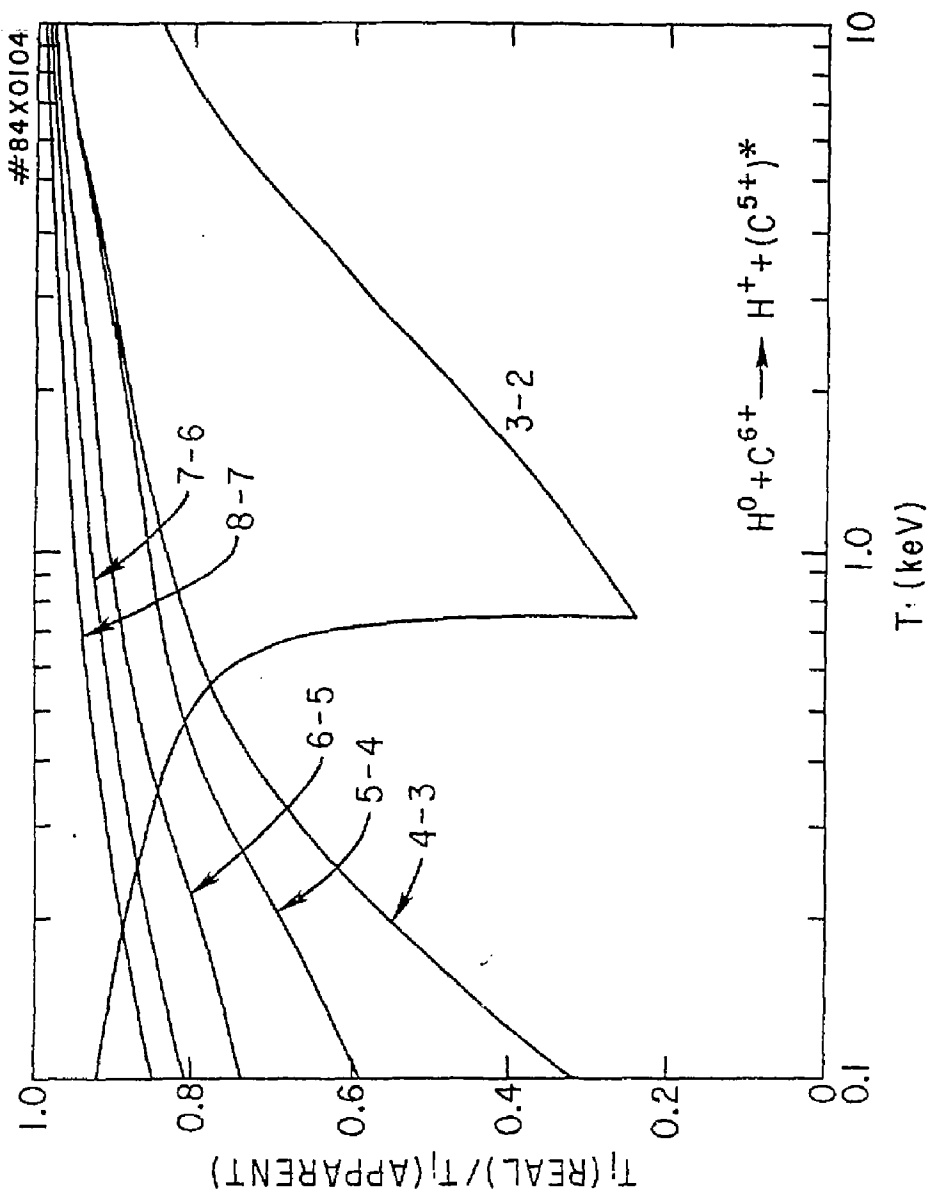


FIG. 14

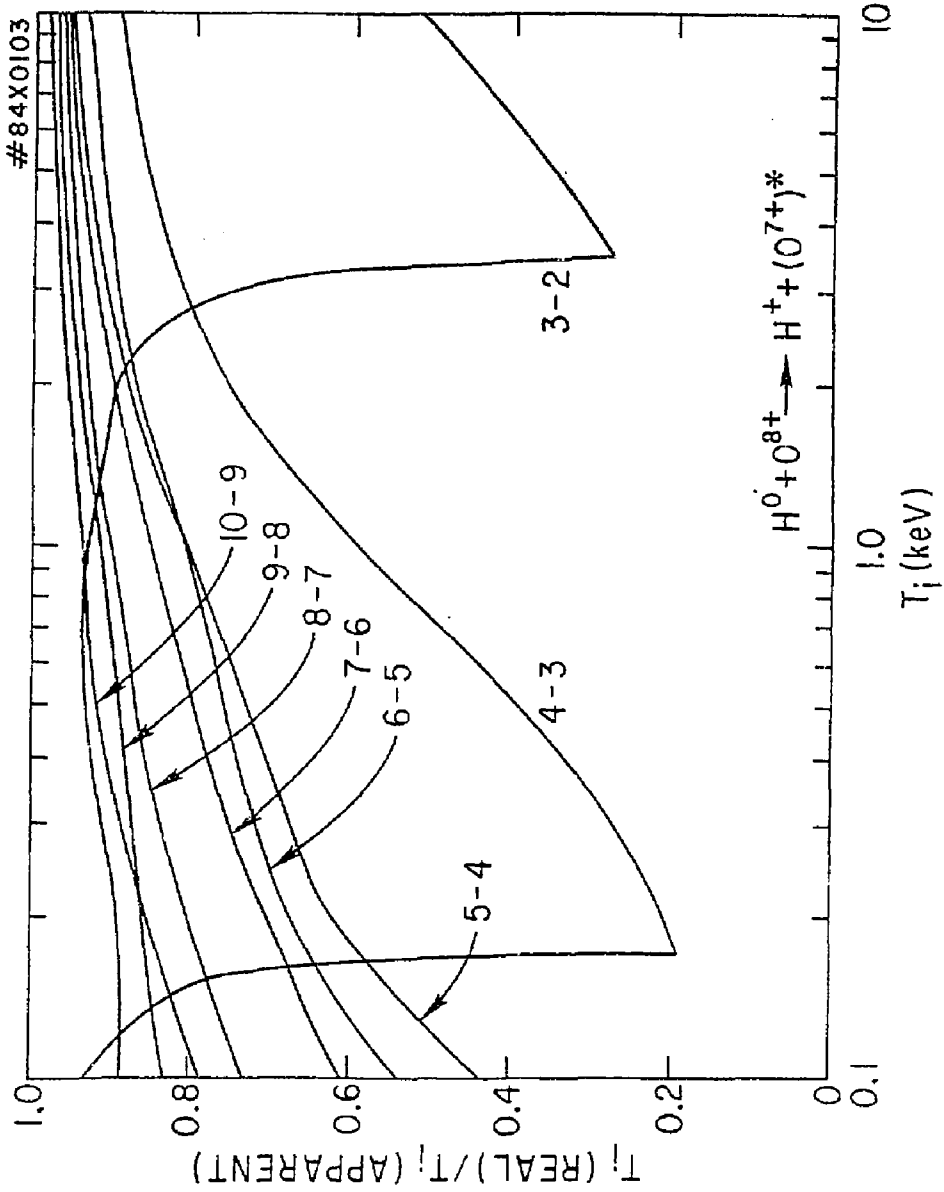


FIG. 15

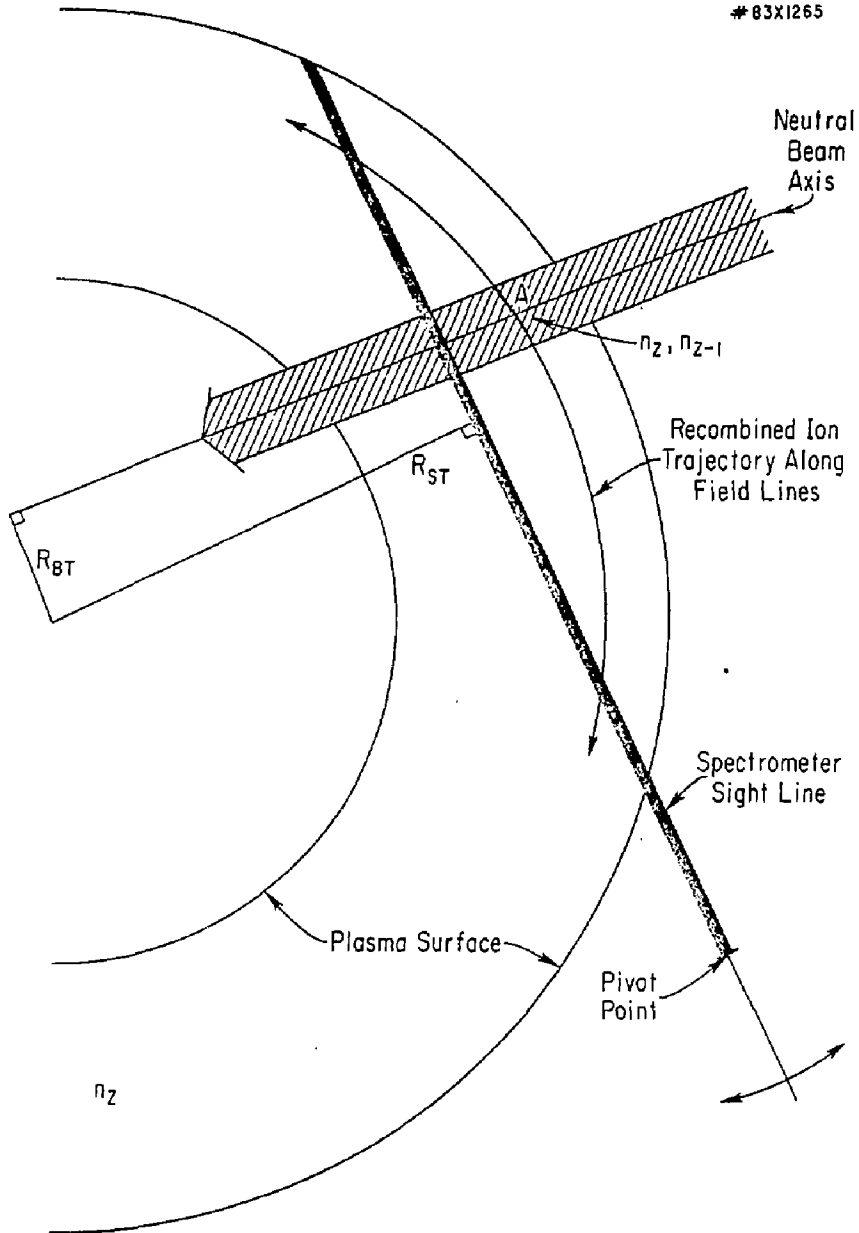
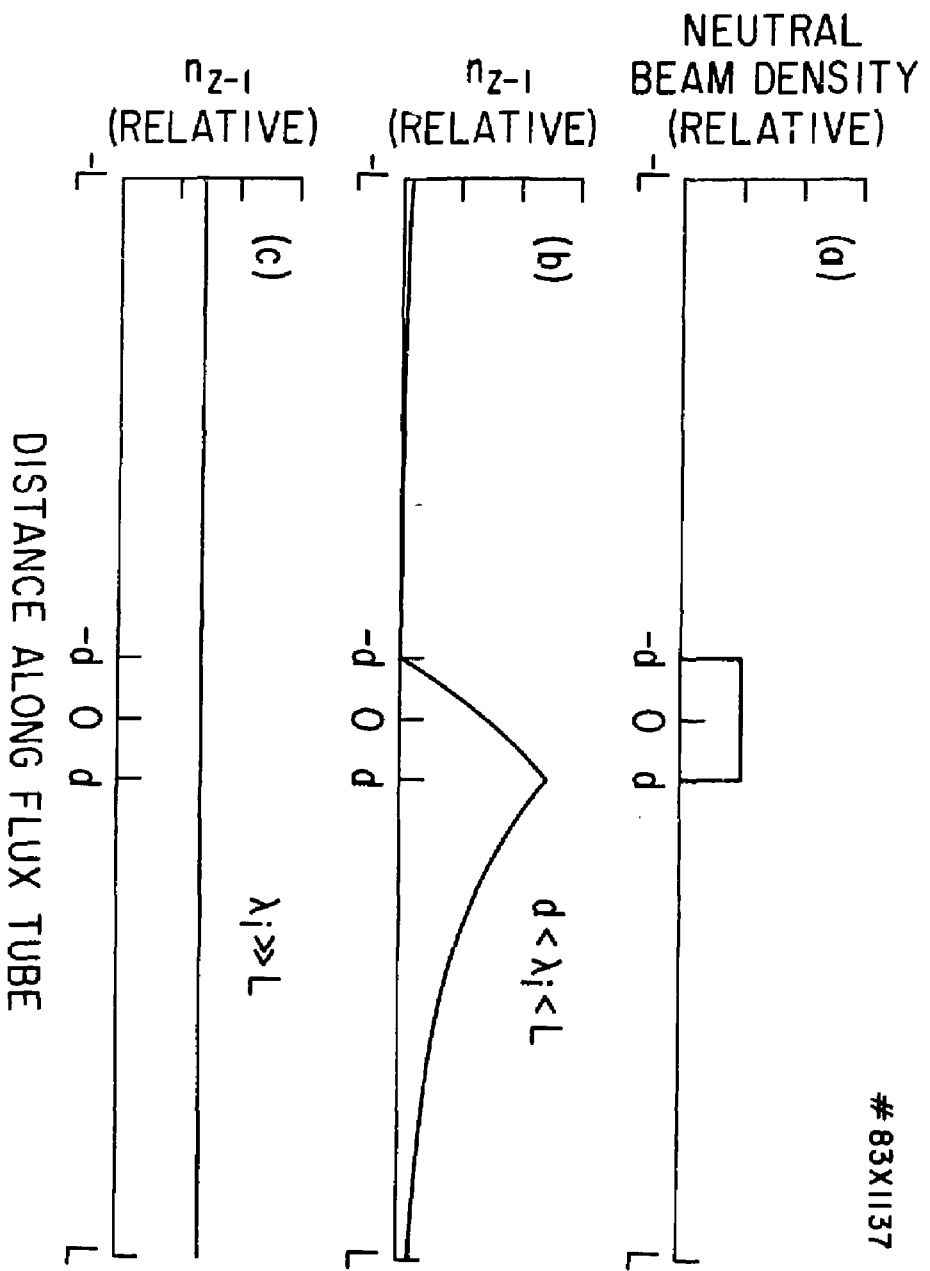


Fig. 16



# 83X1137

Fig. 17



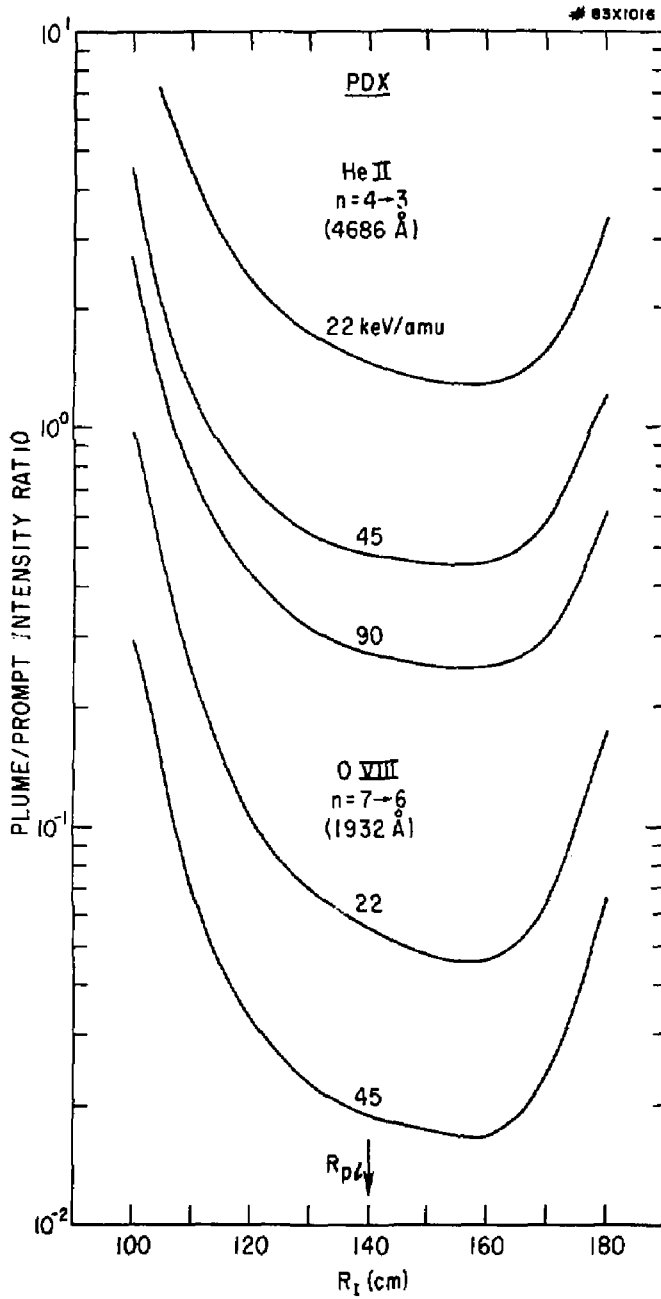


Fig. 18

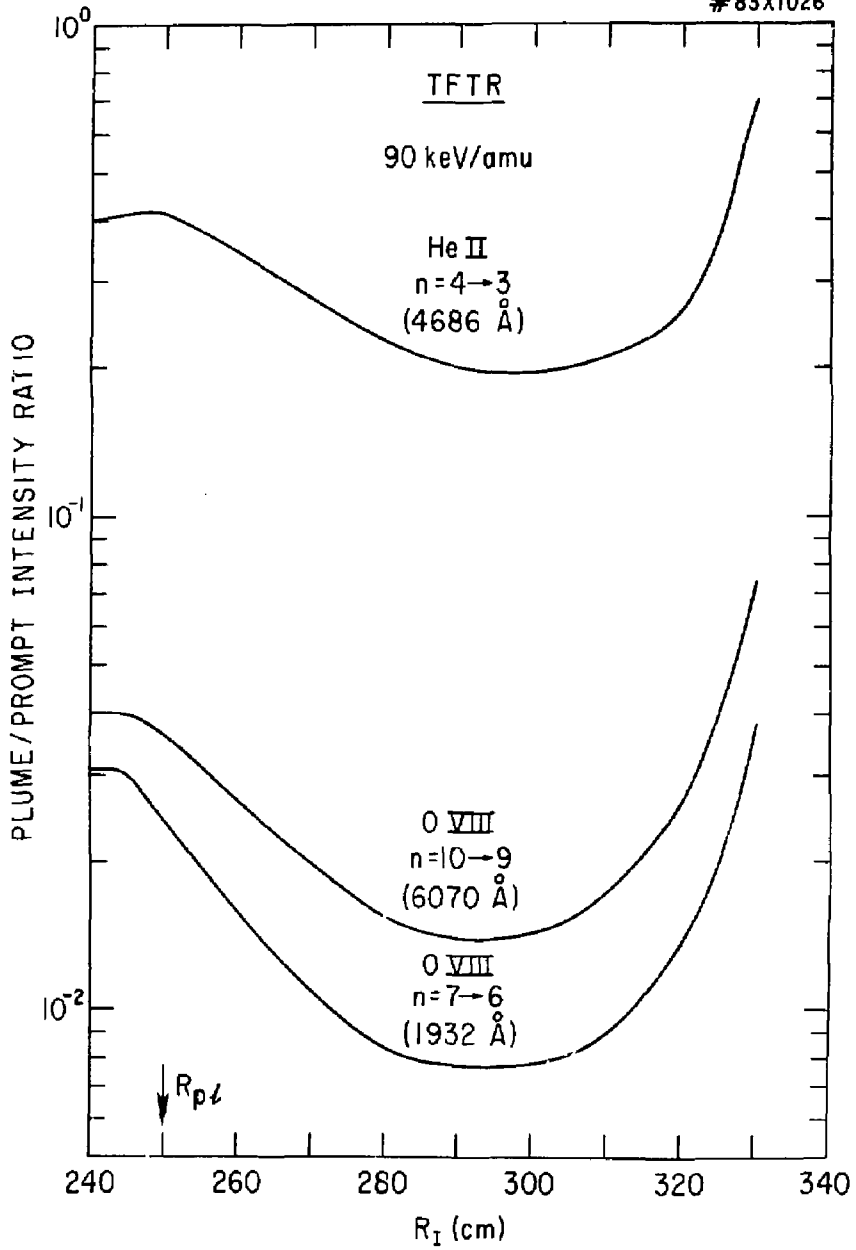


Fig. 19

#83X1110

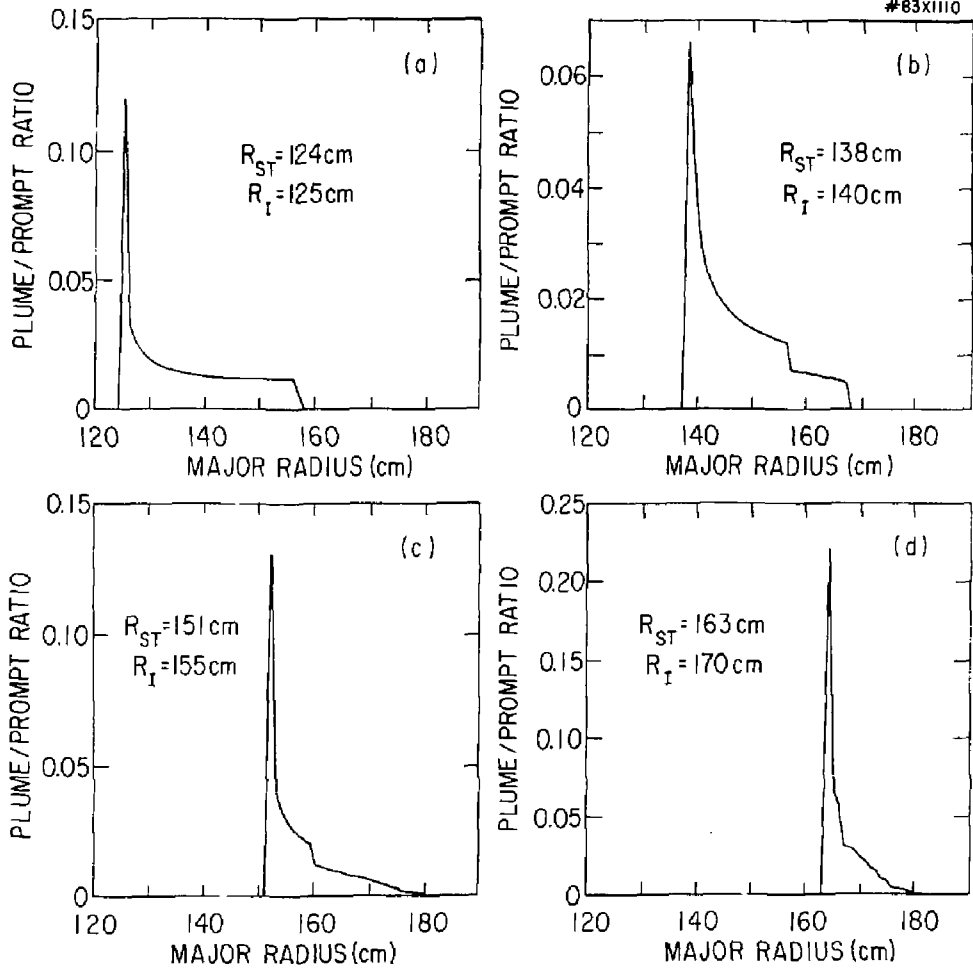


Fig. 20

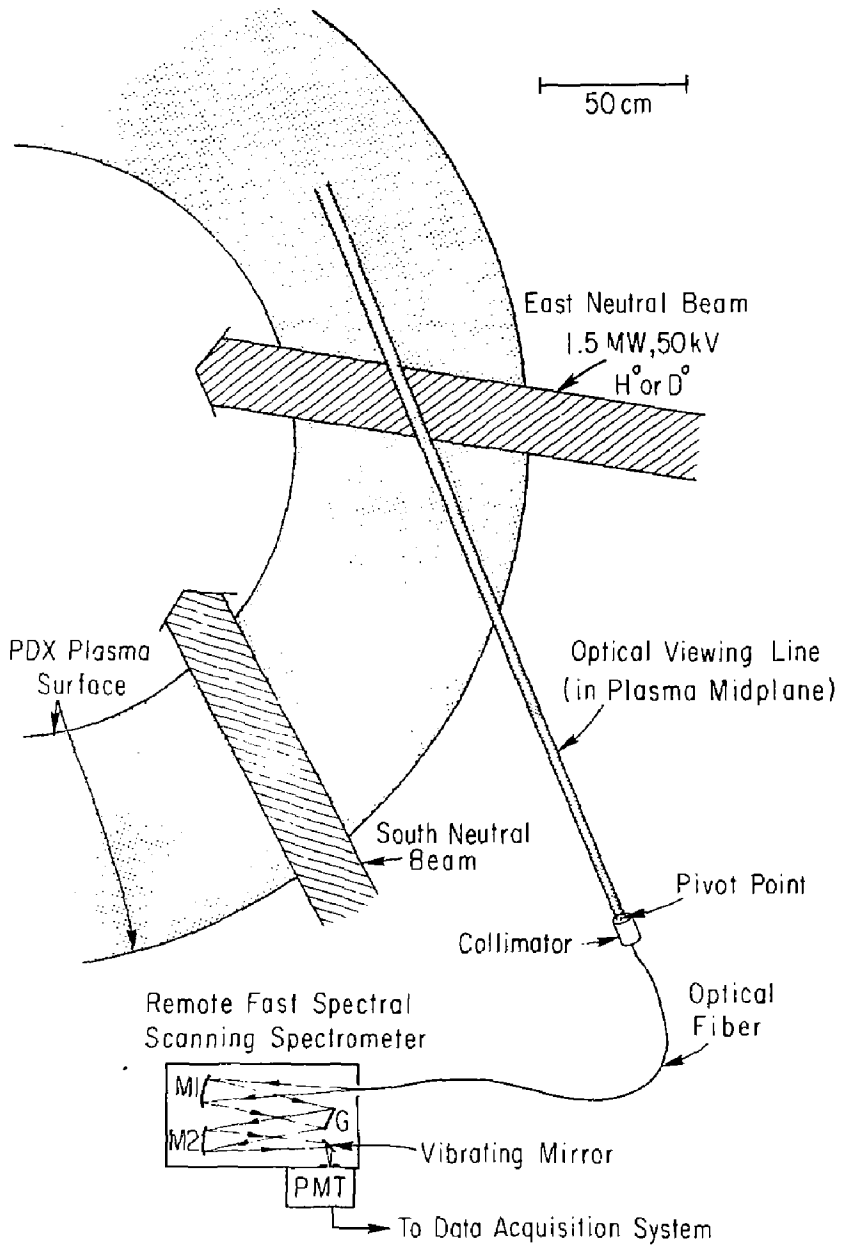


Fig. 21

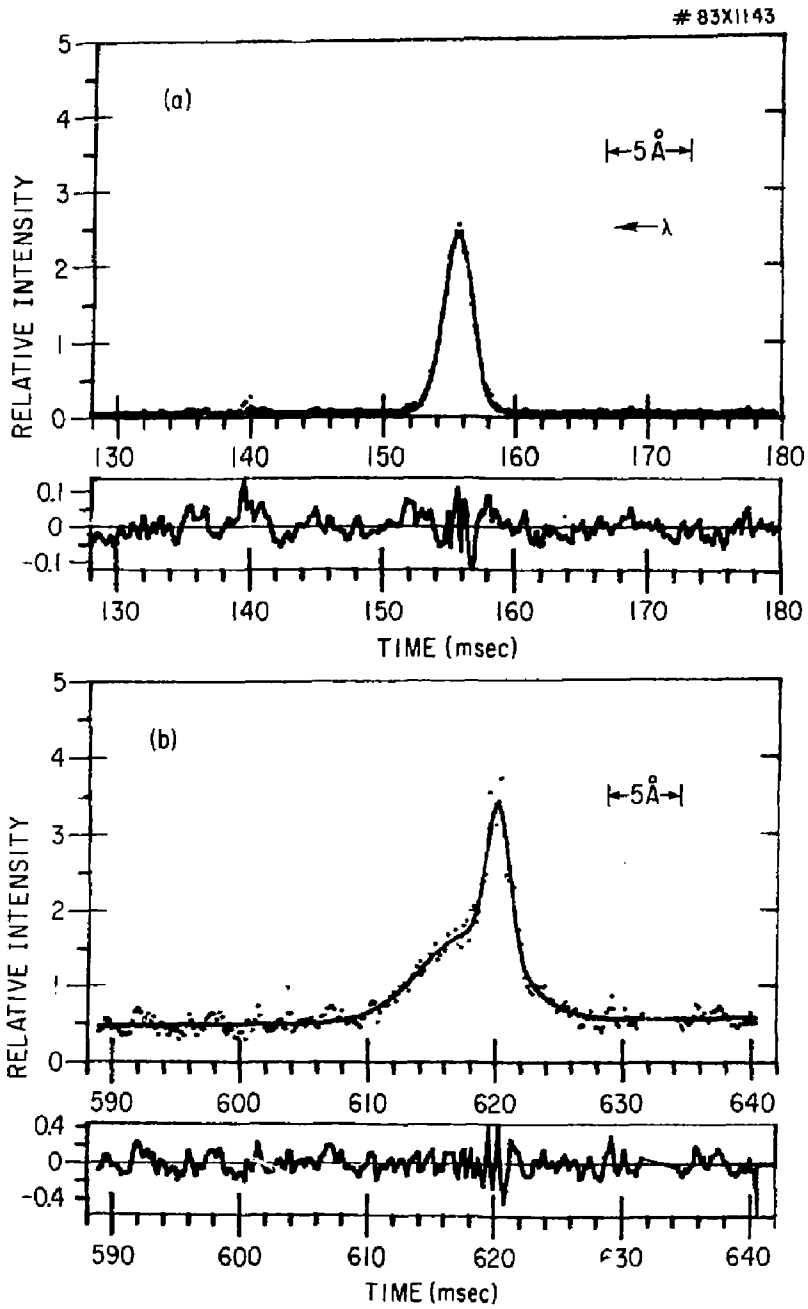


Fig. 22

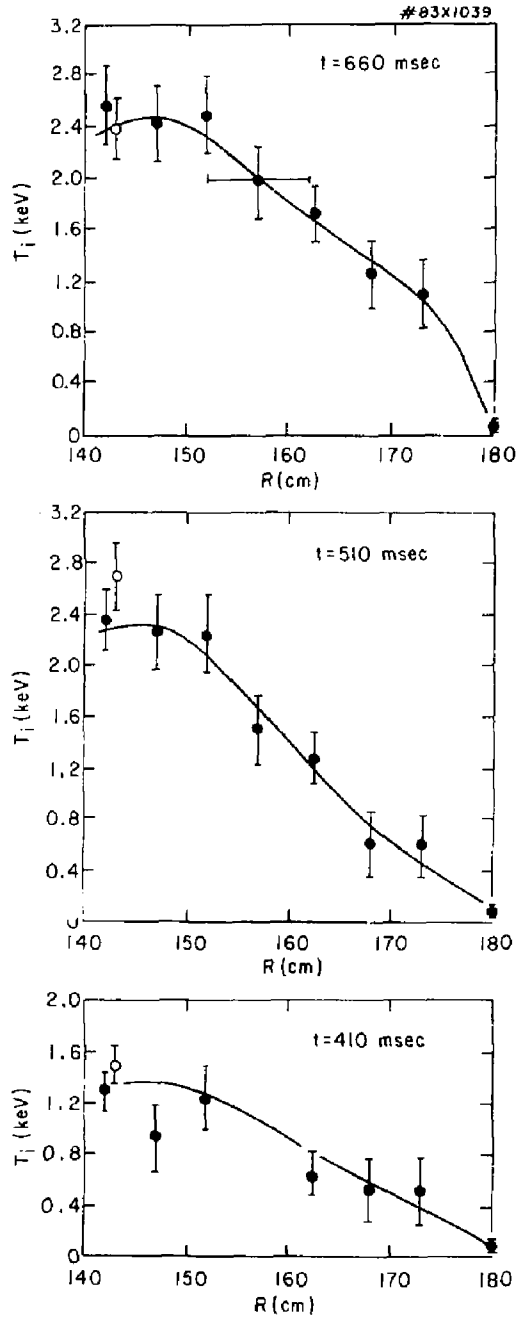


Fig. 23

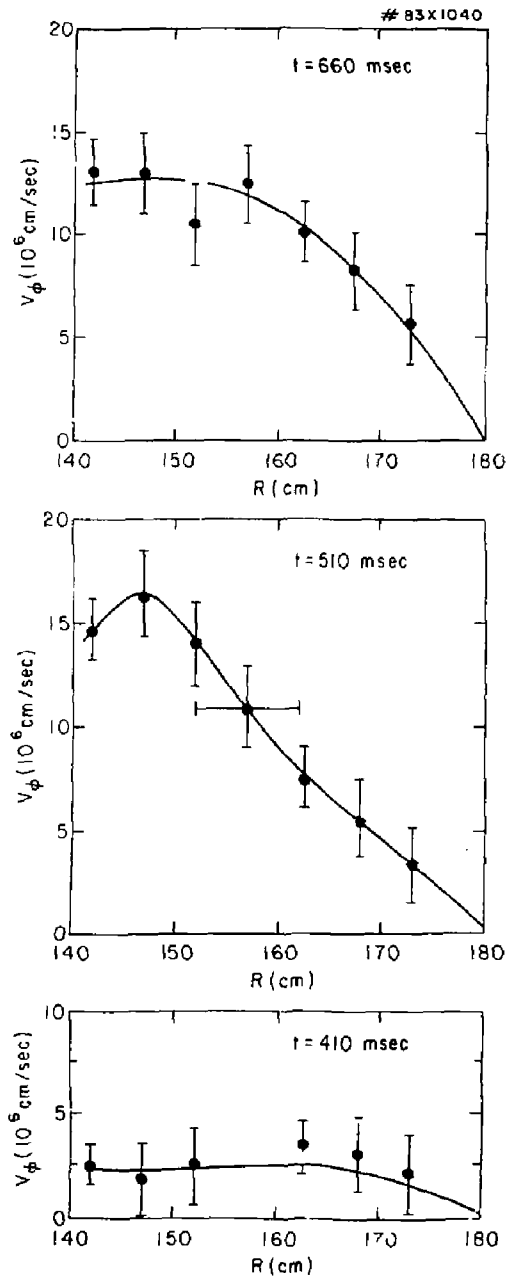


Fig. 24

# 83X1142

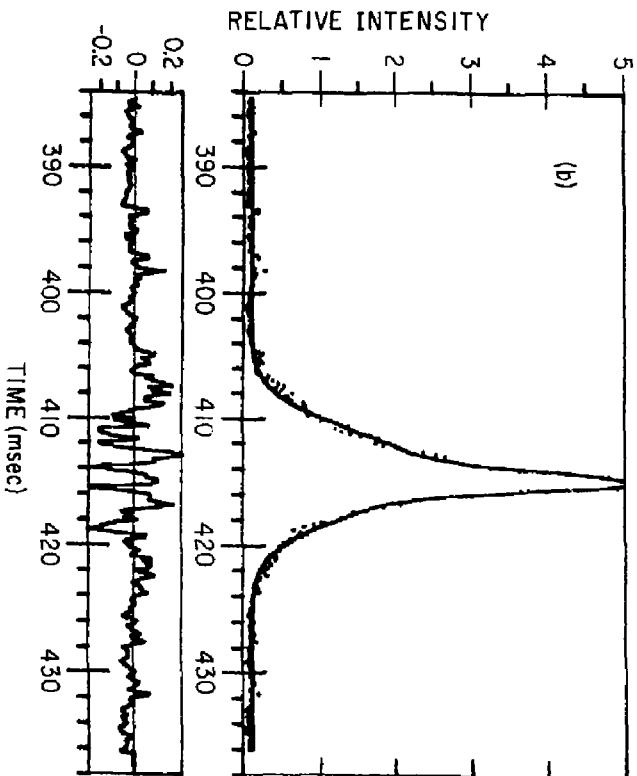
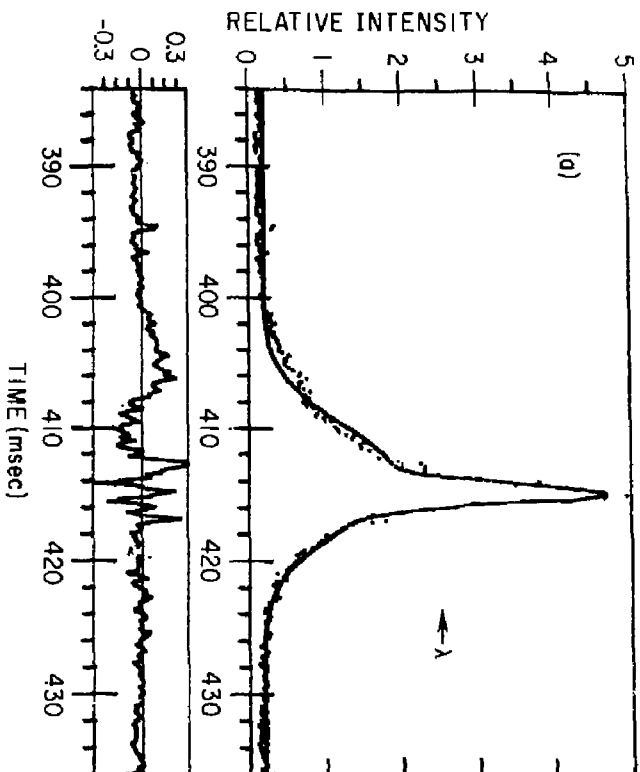


Fig. 25



# 83X1136

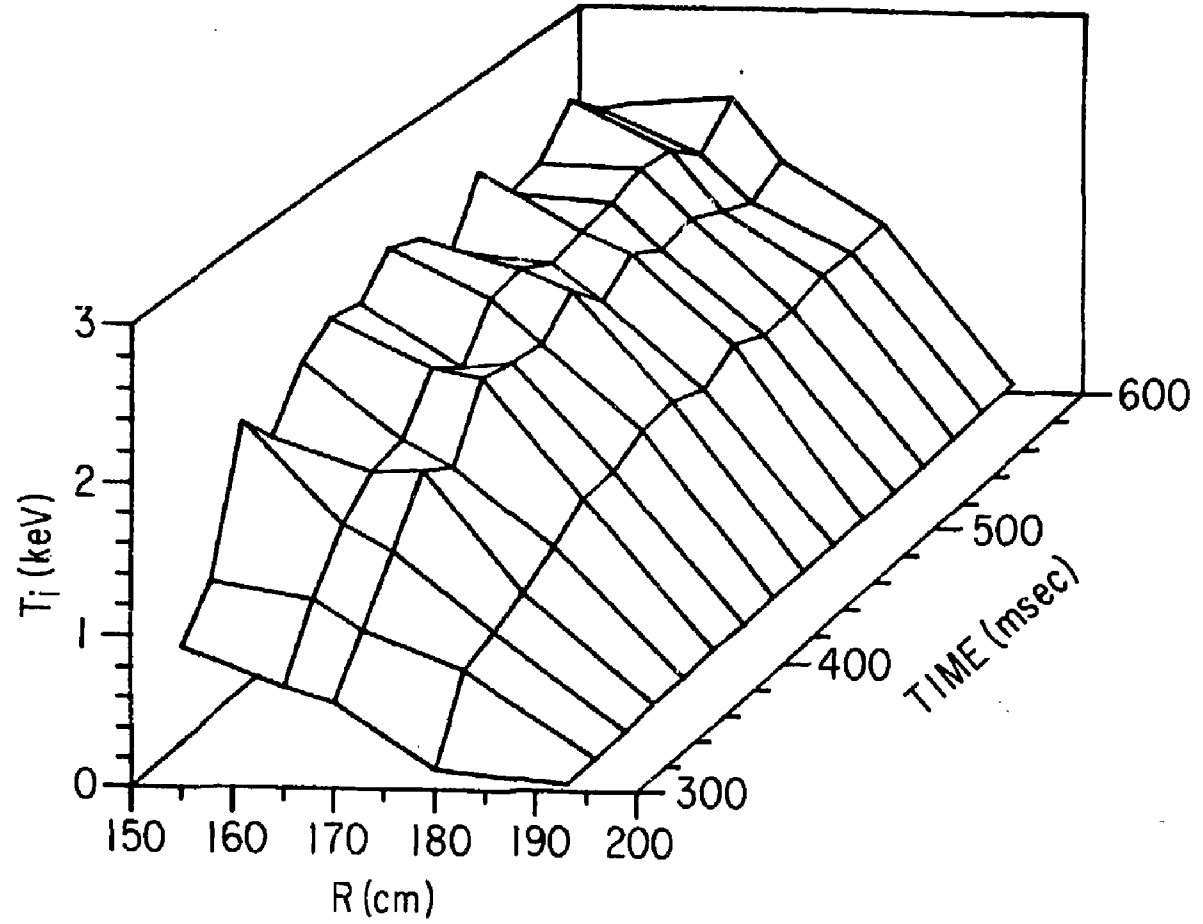


Fig. 26

EXTERNAL DISTRIBUTION IN ADDITION TO TIC UC-20

Plasma Res Lab, Austra Nat'l Univ, AUSTRALIA  
 Dr. Frank J. Footoni, Univ of Wollongong, AUSTRALIA  
 Prof. I.R. Jones, Flinders Univ., AUSTRALIA  
 Prof. M.H. Brennan, Univ Sydney, AUSTRALIA  
 Prof. F. Cap, Inst Theo Phys, AUSTRIA  
 Prof. Frank Verheest, Inst theoretische, BELGIUM  
 Dr. D. Palumbo, Dg XII Fusion Prog, BELGIUM  
 Ecole Royale Militaire, Lab de Phys Plasmas, BELGIUM  
 Dr. P.H. Sakanaka, Univ Estadual, BRAZIL  
 Dr. C.R. James, Univ of Alberta, CANADA  
 Prof. J. Teichmann, Univ of Montreal, CANADA  
 Dr. H.M. Skarsgard, Univ of Saskatchewan, CANADA  
 Prof. S.R. Greenivasan, University of Calgary, CANADA  
 Prof. Tudor W. Johnston, INRS-Energie, CANADA  
 Dr. Hanne Bernard, Univ British Columbia, CANADA  
 Dr. M.P. Bachynski, MPB Technologies, Inc., CANADA  
 Zhengwu Li, SW Inst Physics, CHINA  
 Librarian, Tsing Hua University, CHINA  
 Librarian, Institute of Physics, CHINA  
 Inst Plasma Phys, Academia Sinica, CHINA  
 Dr. Peter Lukac, Komenskeho Univ, CZECHOSLOVAKIA  
 The Librarian, Culham Laboratory, ENGLAND  
 Prof. Schatzman, Observatoire de Nice, FRANCE  
 J. Radet, CEN-BP6, FRANCE  
 AM Dupas Library, AM Dupas Library, FRANCE  
 Dr. Tom Muat, Academy Bibliographic, HONG KONG  
 Preprint Library, Cent Res Inst Phys, HUNGARY  
 Dr. S.K. Trehan, Panjab University, INDIA  
 Dr. Indre, Mohan Lal Das, Banaras Hindu Univ, INDIA  
 Dr. L.K. Chevda, South Gujarat Univ, INDIA  
 Dr. R.K. Chhajlani, Var Ruchi Marg, INDIA  
 P. Kow, Physical Research Lab, INDIA  
 Dr. Phillip Rosenau, Israel Inst Tech, ISRAEL  
 Prof. S. Cuperman, Tel Aviv University, ISRAEL  
 Prof. G. Rostagni, Univ Di Padova, ITALY  
 Librarian, Int'l Ctr Theo Phys, ITALY  
 Miss Ciella De Palo, Assoc EURATOM-CNEN, ITALY  
 Biblioteca, del CNR EURATOM, ITALY  
 Dr. M. Yamato, Toshiba Res & Dev, JAPAN  
 Prof. M. Yoshikawa, JAERI, Tokai Res Est, JAPAN  
 Prof. T. Uchida, University of Tokyo, JAPAN  
 Research Info Center, Nagoya University, JAPAN  
 Prof. Kyoji Nishikawa, Univ of Hiroshima, JAPAN  
 Prof. Sigeru Mori, JAERI, JAPAN  
 Library, Kyoto University, JAPAN  
 Prof. Ichiro Kawakami, Nihon Univ, JAPAN  
 Prof. Satoshi Itoh, Kyushu University, JAPAN  
 Tech Info Division, Korea Atomic Energy, KOREA  
 Dr. R. England, Ciudad Universitaria, MEXICO  
 Bibliotheek, Fom-Inst Voor Plasma, NETHERLANDS  
 Prof. B.S. Lilley, University of Waikato, NEW ZEALAND  
 Dr. Suresh C. Sharma, Univ of Calabar, NIGERIA  
 Prof. J.A.C. Cabral, Inst Superior Tech, PORTUGAL  
 Dr. Octavian Petrus, ALI GUZA University, ROMANIA  
 Prof. M.A. Hellberg, University of Natal, SO AFRICA  
 Dr. Johan de Villiers, Atomic Energy Bd, SO AFRICA  
 Fusion Div. Library, JEN, SPAIN  
 Prof. Hans Wilhelmson, Chalmers Univ Tech, SWEDEN  
 Dr. Lennart St. flo, University of UMEA, SWEDEN  
 Library, Royal Inst Tech, SWEDEN  
 Dr. Erik T. Karlson, Uppsala Universitet, SWEDEN  
 Centre de Recherches, Ecole Polytech Fed, SWITZERLAND  
 Dr. W.L. Hulse, Nat'l Bur Stand, USA  
 Dr. W.M. Stacey, Georg Inst Tech, USA  
 Dr. S.T. Wu, Univ Alabama, USA  
 Prof. Norman L. Olsson, Univ S Florida, USA  
 Dr. Benjamin Ma, Iowa State Univ, USA  
 Prof. Magne Kristiansen, Texas Tech Univ, USA  
 Dr. Raymond Askew, Auburn Univ, USA  
 Dr. V.T. Tolok, Kharkov Phys Tech Ins, USSR  
 Dr. D.D. Ryutov, Elberlan Acad Sci, USSR  
 Dr. G.A. Ellisev, Kurchatov Institute, USSR  
 Dr. V.A. Glukhikh, Inst Electro-Physical, USSR  
 Institute Gen. Physics, USSR  
 Prof. T.J. Boyd, Univ College N Wales, WALES  
 Dr. K. Schindler, Ruhr Universitat, W. GERMANY  
 Nuclear Res Estab, Julich Ltd, W. GERMANY  
 Librarian, Max-Planck Institut, W. GERMANY  
 Dr. H.J. Kaeppeler, University Stuttgart, W. GERMANY  
 Bibliothek, Inst Plasmeforschung, W. GERMANY